

## CO-dark molecular gas traced by HCO<sup>+</sup> in the diffuse interstellar medium

DANIEL R. RYBARCZYK <sup>1</sup>, MICHAEL P. BUSCH <sup>2,\*</sup>, J. R. DAWSON <sup>3,4</sup>, MIN-YOUNG LEE <sup>5,6</sup> AND GAN LUO <sup>7</sup>

<sup>1</sup>University of Wisconsin–Madison, Department of Astronomy, 475 N Charter St, Madison, WI 53703, USA

<sup>2</sup>National Radio Astronomy Observatory, 520 Edgemont Road, Charlottesville, VA 22903, USA

<sup>3</sup>School of Mathematical and Physical Sciences and Astrophysics and Space Technologies Research Centre, Macquarie University, Sydney 2109, Australia

<sup>4</sup>Australia Telescope National Facility, CSIRO Space & Astronomy, PO Box 76, Epping, NSW 1710, Australia

<sup>5</sup>Korea Astronomy and Space Science Institute, 776 Daedeok-daero, Daejeon 34055, Republic of Korea

<sup>6</sup>Department of Astronomy and Space Science, University of Science and Technology, 217 Gajeong-ro, Daejeon 34113, Republic of Korea

<sup>7</sup>Institut de Radioastronomie Millimétrique, 300 rue de la Piscine, 38400, Saint-Martin d’Hères, France

### ABSTRACT

A classic problem in the study of the interstellar medium (ISM) is the near-invisibility of molecular hydrogen (H<sub>2</sub>) in cold environments. Observations of CO emission are typically used to indirectly trace H<sub>2</sub>, but a significant fraction of H<sub>2</sub> in the diffuse ISM is not associated with any detectable CO emission (“CO-dark” molecular gas). Meanwhile, observations of HCO<sup>+</sup> absorption trace nearly all of the H<sub>2</sub> in diffuse directions. In particular, a kinematically broad HCO<sup>+</sup> absorption signature traces extremely diffuse, CO-dark H<sub>2</sub>. We have used sensitive observations of HCO<sup>+</sup>, CO, and atomic hydrogen (HI) in absorption to constrain the properties of such diffuse molecular gas in five directions. The diffuse molecular gas revealed by broad HCO<sup>+</sup> absorption has a lower fraction of cold HI ( $f_{\text{CNM}} = 0.38^{+0.28}_{-0.27}$ ) and a lower fraction of hydrogen in H<sub>2</sub> ( $f_{\text{mol}} = 0.09^{+0.06}_{-0.03}$ ) than gas traced by CO in the same directions. We detect almost no CO absorption from the gas traced by broad HCO<sup>+</sup> absorption. We constrain the CO abundance relative to H<sub>2</sub> to be  $\lesssim 10^{-6}$ – $10^{-5}$  for gas traced by both broad and narrow HCO<sup>+</sup> absorption, consistent with chemical model predictions for the diffuse ISM. We further show that neither CO emission nor absorption is likely to be detected where  $N(\text{H}_2) \lesssim \text{few} \times 10^{19} \text{ cm}^{-2}$  — a result of both the low CO abundance and the low H<sub>2</sub> column — while HCO<sup>+</sup> absorption is readily detected for  $N(\text{H}_2) \gtrsim \text{few} \times 10^{18} \text{ cm}^{-2}$ . These results demonstrate that even modest amounts of cold HI can bear H<sub>2</sub>, providing critical constraints on the HI-to-H<sub>2</sub> transition in the ISM.

### 1. INTRODUCTION

Molecular hydrogen (H<sub>2</sub>) is the most abundant molecule in the interstellar medium (ISM) and plays a key role in chemistry and star formation (e.g., Bigiel et al. 2008). Yet, because H<sub>2</sub> lacks a permanent dipole moment and because of the large energy spacing between the two lowest rotational transitions, it is extremely difficult to observe directly at low temperatures. Instead, alternative tracers in emission and absorption are used to investigate the distribution, kinematics, and structure of the molecular ISM.

The CO molecule is one of the most commonly used tracers of the molecular content of galaxies because of its

high abundance<sup>1</sup> and its brightness in molecular clouds. Yet, the relationship between the integrated CO emission and the H<sub>2</sub> column density, summarized with the  $X_{\text{CO}}$  factor,  $X_{\text{CO}} = N(\text{H}_2)/W_{\text{CO}}$ , varies between and within galaxies (see review by Bolatto et al. 2013, and references therein).

Additionally, a significant quantity of “CO-dark” molecular gas (that is, H<sub>2</sub> not traced by CO emission) exists in diffuse ( $A_V \lesssim 1 \text{ mag}$ ) environments (e.g., Allen et al. 2015; Liszt et al. 2019; Busch et al. 2019, 2021; Liszt & Gerin 2023a; Luo et al. 2024). Two important tracers of this diffuse molecular component are OH emission and HCO<sup>+</sup> absorption (Liszt et al. 2019; Busch et al. 2021; Liszt & Gerin 2023a). Since both OH and

Corresponding author: Daniel R. Rybarczyk  
rybarczyk@astro.wisc.edu

\* Jansky Fellow of the National Radio Astronomy Observatory

<sup>1</sup> Throughout the text, we refer to the “abundance” of different molecular species as the ratio between molecular column density to the H<sub>2</sub> column density, unless otherwise specified.

HCO<sup>+</sup> are known to have nearly fixed abundances with respect to H<sub>2</sub> in diffuse environments (Liszt & Lucas 2000; Xu et al. 2016; Nguyen et al. 2018; Liszt & Gerin 2023b), they are considered to be excellent tracers of diffuse molecular gas.

Intriguingly, a kinematically-broad CO-dark spectral signature has recently been detected in both OH emission (Busch et al. 2021) and HCO<sup>+</sup> absorption (Liszt & Lucas 2000; Rybarczyk et al. 2022). The molecular gas traced by these signatures has different temperature and density properties than “CO-bright” gas detected along the same lines of sight (Liszt & Lucas 2000; Liszt & Pety 2012; Busch et al. 2021; Rybarczyk et al. 2022). Busch et al. (2021) showed that broad OH emission traces large-scale Galactic velocity structure. Specifically, they argued that the OH emission was evidence for a thick ( $\sim 200$  pc) disk of CO-dark diffuse molecular gas in the Outer Galaxy, invisible to canonical Galactic CO surveys like Dame et al. (2001). Meanwhile, Rybarczyk et al. (2022) argued that the molecular gas traced by broad HCO<sup>+</sup> absorption probes the earliest stages of molecule formation in the Galactic ISM, where the molecular fraction of hydrogen,  $f_{\text{mol}} = 2n_{\text{H}_2}/n_{\text{H}}$ , is  $\lesssim 10\%$ . Interestingly, previous independent analyses of these two signatures have suggested that both could be explained by the presence of molecular gas with a mean H<sub>2</sub> number density of  $n \sim 10^{-3}$ – $10^{-2}$  cm<sup>-3</sup> (Liszt & Lucas 2000; Busch et al. 2021), although observations do not rule out the presence of unresolved higher-density clumps. These observations provide valuable constraints on the physical properties of the reservoir of CO-dark molecular gas that exists in the diffuse ISM.

Atomic hydrogen (HI) provides the raw material for the formation of H<sub>2</sub> (which occurs primarily on the surfaces of dust grains; see Cazaux & Tielens 2002, and references therein), so characterizing the properties of HI is key to understanding how molecule formation commences. HI exists as a multiphase medium, with gas distributed between a warm, diffuse phase (the warm neutral medium, “WNM”); a colder, denser phase (the cold neutral medium, “CNM”); and a thermally unstable phase at intermediate temperature and density (the unstable neutral medium, “UNM;” e.g., Murray et al. 2018; McClure-Griffiths et al. 2023, and references therein). The CNM is particularly important in fueling molecule formation, since it provides the number and column densities necessary to (a) form molecules at an appreciable rate, and (b) shield them from photodissociation. It is unsurprising, therefore, that molecular gas is found preferentially in directions with a high fraction of HI in the form of CNM (Stanimirović et al. 2014;

Nguyen et al. 2019; Rybarczyk et al. 2022; Park et al. 2023; Hafner et al. 2023).

Yet, Rybarczyk et al. (2022) showed that the HI associated with broad, CO-dark HCO<sup>+</sup> absorption has a systematically lower CNM fraction than the HI associated with CO-bright molecular gas, suggesting that molecules can form in environments with significantly lower CNM column densities than previously thought (e.g., Stanimirović et al. 2014). In fact, in some directions the broad CO-dark HCO<sup>+</sup> signature traces nearly all velocities where HI is detected in absorption — a result that was also found in the earlier work of Liszt & Lucas (2000). This is in contrast to the behavior of CO-bright gas, which is generally coincident only with the coldest, optically thickest HI (Nguyen et al. 2019; Park et al. 2023; Hafner et al. 2023). Even more surprising, Busch et al. (2021) showed that, in certain directions, broad OH emission traces nearly all velocities where HI is detected in *emission*. Whereas HI absorption arises primarily from the CNM (and some UNM), the HI emission arises from a mixture of CNM, UNM, and WNM.

Despite the intriguing results presented by Liszt & Lucas (2000), Busch et al. (2021), and Rybarczyk et al. (2022), these investigations of the CO-dark diffuse molecular gas were limited in scope. For example, because Busch et al. (2021) investigated the atomic gas in the diffuse ISM using only HI emission, they were unable to investigate the multiphase HI properties in detail — the CNM, UNM, and WNM can only be reliably separated using the combination of HI emission and absorption (e.g., Heiles & Troland 2003). Meanwhile, the classification of CO-dark gas used by Rybarczyk et al. (2022) was based on CO emission data from Dame et al. (2001), but the definition of “CO-dark” always implicitly depends on CO sensitivity (e.g., Donate & Magnani 2017). Indeed, Li et al. (2018) showed that more sensitive CO emission observations often detected diffuse CO where Dame et al. (2001) did not, leaving open the possibility that the non-detections in Rybarczyk et al. (2022) were merely a consequence of sensitivity. Moreover, the Rybarczyk et al. (2022) HCO<sup>+</sup> absorption observations probed pencil-beam sightlines, which trace much smaller physical scales on the plane of the sky than the relatively large CO emission beams, so their CO and HCO<sup>+</sup> observations were not necessarily probing the same molecular gas structures. Finally, Liszt & Lucas (2000) did not compare their broad HCO<sup>+</sup> absorption observations to observations of CO in the same directions. Therefore, high-sensitivity observations of HCO<sup>+</sup>, CO, and HI (in absorption) at a comparable spatial resolution are essential to quantify the physical properties and evolution of diffuse molecular gas.

**Table 1.** Categories of molecular line observations

Category	HCO <sup>+</sup> absorption	CO absorption	CO emission	Description
1	No	No	No	Atomic
2	Yes	No	No	CO-dark
3	Yes	Yes	No	CO-dark*
4	Yes	Yes	Yes	CO-bright

In this work, we directly compare sensitive observations of HCO<sup>+</sup>, CO, and HI in absorption in five directions where broad HCO<sup>+</sup> absorption has previously been detected (Luo et al. 2020; Rybarczyk et al. 2022, 2023). We present new CO absorption observations in three of these directions and new HI observations in two of these directions. We also use archival CO absorption observations in three directions (including one direction that we re-observed here for improved sensitivity; Luo et al. 2020) and archival HI absorption observations in three directions (Murray et al. 2015, 2018; Rybarczyk et al. 2022 previously discussed the HI and HCO<sup>+</sup> in these three directions). The CO absorption observations trace CO at almost exactly the same angular scale as the HCO<sup>+</sup> observations, and with much greater CO column density sensitivity than observations of CO emission (e.g., Liszt & Lucas 1998), allowing us to place more reliable constraints on the column densities and abundances of CO. In an effort to be consistent with the parlance used in the existing literature (which has focused largely on CO emission) while incorporating these new observations, we explicitly define different categories of gas based on the presence or absence of HCO<sup>+</sup> absorption, CO absorption, and CO emission (Table 1). In particular, we use “CO-dark” to describe molecular gas (as revealed by HCO<sup>+</sup> absorption) with no associated CO emission *or* absorption, while we use “CO-dark\*” to refer to molecular gas with associated CO absorption but no associated CO emission. We use “CO-bright” to describe gas with both CO absorption and CO emission.<sup>2</sup>

<sup>2</sup> In other works (e.g., Liszt & Pety 2012), a further distinction has been made to characterize CO-bright gas based on the observed brightness of CO relative to the expected brightness given a standard conversion to CO intensity  $W_{\text{CO}} = N(\text{H}_2)/(2 \times 10^{20} [\text{cm}^{-2} (\text{K km s}^{-1})^{-1}])$  (e.g., Bolatto et al. 2013, and references therein). Since we are focused primarily on CO absorption here, we do not make such a distinction in this work, and instead adopt the broader CO-bright definition in Table 1. We also do not detect CO emission without absorption in this work, so do not make a category for such gas.

Meanwhile, the HI absorption observations allow us to constrain the multiphase properties of the atomic gas, also at the tiny angular scales probed by pencil-beam absorption (though the background source structure may be slightly different between the 3 mm molecular absorption and 21 cm atomic absorption data). Together, these complementary observations make it possible to characterize and compare the physical properties of the diffuse molecular, dense molecular, and cold atomic gas, on matched spatial scales and at unprecedented sensitivity.

The paper is structured as follows. In Section 2, we present the new and archival observations of HCO<sup>+</sup> and CO absorption from the Northern Extended Millimetre Array interferometer (NOEMA) and the Atacama Large Millimeter/submillimeter Array (ALMA) and HI absorption from the Karl G. Jansky Very Large Array (VLA). In Section 3, we explain how HCO<sup>+</sup>, CO, and HI absorption spectra are extracted from the interferometric observations, as well as how atomic and molecular column densities are determined from the absorption spectra. We then present the spectra in Section 4 and directly compare the HCO<sup>+</sup>, CO, and HI properties in these directions. In Section 5, we discuss the implications of these results in the context of observational and theoretical studies of molecule formation in the ISM. Finally, we present our conclusions in Section 6.

## 2. OBSERVATIONS

### 2.1. *New and archival molecular line observations with NOEMA*

We have observed the  $J=(1-0)$  transition of CO (115.2712 GHz) in absorption against the background radio continuum sources 3C111, NRAO 530, and J2023+335 (Table 2) with NOEMA (project W21AC). We placed a high-resolution chunk (62.5 kHz channel spacing) in the upper sideband to cover the CO line. While the upper sideband has somewhat poorer sensitivity than the lower sideband, the CO transition is near the highest frequencies observable in NOEMA Band

**Table 2.** Sensitivities and flux densities for our sources

Sightline	$\ell$	$b$	$\sigma_{\tau_{\text{HCO}^+}}$	$\sigma_{\tau_{\text{CO}}}$	$\sigma_{\tau_{\text{HI}}}$	$F_{89}$	$F_{115}$	$E(B - V)$
	deg	deg				Jy	Jy	mag
3C111	161.7	-8.8	0.0012	0.0040	0.0023	1.15/2.25	1.56	$1.117 \pm 0.056$
NRAO 530	12.0	10.8	0.0026	0.0067	0.0017	1.97	1.60	$0.511 \pm 0.012$
J2023+335	73.1	-2.4	0.0009	0.0044	0.0027	1.01	2.04	$1.248 \pm 0.012$
3C454.3	86.1	-38.2	0.0008	0.0024	0.0015	14.34	11.96	$0.104 \pm 0.004$
3C120	190.4	-27.4	0.0050	0.0127	0.0011	3.30	2.46	$0.267 \pm 0.007$

1. The bright sources 3C84, 3C273, 3C345, 3C454.3, and 2013+370 were used as bandpass calibrators<sup>3</sup>. The bandpass was stable across all our observations, and previous work (e.g., Rybarczyk et al. 2022 and earlier work by, e.g., Liszt et al. 2005, 2014, and references therein) has shown that optical depths  $\lesssim 10^{-3}$  can reliably be recovered with NOEMA (and previously the Plateau de Bure interferometer) using similar setups. Targets were observed for 0.4–4.1 hours. All data reduction steps were done using the CLIC and MAPPING programs within the GILDAS software collection (Pety 2005; Gildas Team 2013)<sup>4</sup>. We performed self-calibration using MAPPING’s built-in tool, since our sources all had flux densities  $\gtrsim 1$  Jy (Table 2).

HCO<sup>+</sup> absorption has previously been observed with NOEMA toward the bright background sources 3C111, J2023+335, and NRAO530. Rybarczyk et al. (2023) presented HCO<sup>+</sup> observations toward J2023+335 and NRAO530. We use their HCO<sup>+</sup> absorption spectra here. Rybarczyk et al. (2022) presented HCO<sup>+</sup> observations toward 3C111 (“3C111A” in their work). Here we have obtained additional, more-sensitive HCO<sup>+</sup> absorption observations in the direction of 3C111 (project W24BG) using an identical setup to that used by Rybarczyk et al. (2022). We placed the HCO<sup>+</sup>  $J=(1-0)$  line (89.1885 GHz) in a high resolution chunk (62.5 kHz channel spacing) in the lower sideband to ensure maximum sensitivity and observed 3C111 for 3.4 hours. The final HCO<sup>+</sup> absorption spectrum toward 3C111 was calculated by combining the spectrum presented by Rybarczyk et al. (2022) with our new observations (weighted by the inverse-square of the noise in the HCO<sup>+</sup> absorption spectra). As with CO, all reduction steps (includ-

ing self-calibration) were carried out using the CLIC and MAPPING programs in GILDAS.

Table 2 lists the coordinates, 89 GHz and 115 GHz flux densities ( $F_{89}$  and  $F_{115}$ ; the difference between the flux densities at 89 GHz and 115 GHz are due both to the continuum spectral index as well as changes in the brightness of the background sources over time), and CO and HCO<sup>+</sup> optical depth sensitivities achieved in the direction of our background sources. We present the CO and HCO<sup>+</sup> absorption spectra at 0.4 km s<sup>-1</sup> velocity resolution in Figure 1 and discuss the spectra in Section 4.

## 2.2. Archival molecular line observations with ALMA

Luo et al. (2020) observed the  $J=(1-0)$  transition of CO in absorption using the Atacama Large Millimeter/submillimeter Array (ALMA) toward 3C120, 3C454.3, and NRAO530 (2015.1.00503.S). Meanwhile, both Luo et al. (2020) (2015.1.00503.S) and Rybarczyk et al. (2022) (2018.1.00585.S) observed the  $J=(1-0)$  transition of HCO<sup>+</sup> in absorption with ALMA toward 3C120 and 3C454.3. These ALMA Band 3 observations are discussed in detail by Luo et al. (2020) and Rybarczyk et al. (2022).

Here we use the CO absorption spectra obtained by Luo et al. (2020) toward 3C120 and 3C454.3. For NRAO530, we combine the Luo et al. (2020) CO absorption spectra with the new CO absorption spectra observed here (Section 2.1), taking a weighted mean (weighted by the inverse square of the noise in  $e^{-\tau}$ ). Similarly, for 3C120 and 3C454.3, we combine the HCO<sup>+</sup> absorption spectra from Luo et al. (2020) and Rybarczyk et al. (2022), again taking a weighted mean. We smooth all ALMA absorption spectra to 0.4 km s<sup>-1</sup> velocity resolution. We list the noise levels in the final CO and HCO<sup>+</sup> spectra in these directions in Table 2. The ALMA CO and HCO<sup>+</sup> absorption spectra are shown in Figure 1.

<sup>3</sup> For NOEMA bandpass calibrations with mm absorption present, the relevant absorption is recognized by the pipeline and masked during bandpass calibration.

<sup>4</sup> <https://www.iram.fr/IRAMFR/GILDAS/>

### 2.3. Archival CO emission observations from the CfA 1.2 m telescope

While we focus on CO absorption in this work, we also show archival CO emission spectra from the 1.2 m Millimeter-Wave Telescope at the Center for Astrophysics (Dame et al. 2001; Dame & Thaddeus 2022) toward all five of our sightlines. These spectra have typical noise  $\lesssim 0.2$  K at  $0.65 \text{ km s}^{-1}$  velocity resolution. The angular resolution achieved in these directions was  $\leq 0.25^\circ$ . The CO emission spectra are shown in Figure 1.

### 2.4. New and archival HI absorption and emission observations

We use observations of HI absorption and emission at 1420 MHz in the direction of all five background targets to constrain the properties of the atomic gas. Previously, Murray et al. (2015, 2018) observed HI absorption with the Karl G. Jansky Very Large Array (VLA) toward 3C111 (“3C111A” in their work), 3C120, and 3C454.3 as part of the 21-SPONGE project. They achieved an HI optical depth sensitivity  $(0.9\text{--}1.7) \times 10^{-3}$  in these directions at  $\sim 0.4 \text{ km s}^{-1}$  velocity resolution. They also extracted emission spectra in these directions using the Galactic Arecibo L-Band Feed Array HI survey (GALFA-HI; Peek et al. 2011, 2018). We use the 21-SPONGE spectra for 3C111, 3C120, and 3C454.3 in this work.

We have further observed HI in absorption with the VLA toward J2023+335 and NRAO530 (project 24A-088) with a nearly identical observing setup and reduction process to that used by the 21-SPONGE project (see Murray et al. 2015 for details; we briefly summarize the observations and reduction here). NRAO530 was observed for 0.7 hours. J2023+335 was observed for 6.4 hours in total, spread across two observations lasting 3.1 hours and 3.3 hours, respectively. Both sources were observed in the VLA’s C configuration; we excluded baselines shorter than 300 m to avoid possible contamination from extended or large-scale HI emission. We used three 1.0 MHz bands with 1.95 kHz channel spacing — one band was centered on the HI line, and the other two bands were offset by  $\pm 1.5$  MHz from the HI line. The offset bands were used to perform bandpass calibration via frequency switching to avoid contamination by Galactic HI absorption. 3C286 was used for bandpass calibration for NRAO530 and J2052+3635 was used for bandpass calibration in the direction of J2023+335. The final absorption spectra are shown in Figure 1 and discussed in Section 4. HI optical depth sensitivities at  $0.4 \text{ km s}^{-1}$  velocity resolution are listed in Table 2.

We also extracted the HI emission profiles in these directions using data from the GALFA-HI survey Peek et al. (2011, 2018) for J2023+335 and from the Parkes Galactic All-Sky Survey (GASS; McClure-Griffiths et al. 2009) for NRAO530 using the approach introduced by Heiles & Troland (2003). Essentially, to avoid contamination of the emission spectra by the continuum sources, we extracted the emission spectra using an interpolation technique with nearby pixels (16 pixels separated by 1 to  $\sqrt{2}$  times the half-power beam width; see Heiles & Troland 2003 for a complete description of the technique). This approach is common in previous HI emission-absorption studies (e.g., Heiles & Troland 2003; Stanimirović et al. 2014; Murray et al. 2015).

### 2.5. Reddening measurements

To provide further context for our observations, in Table 2 we also report  $E(B-V)$  measured in each direction by Green et al. (2019). The 3D reddening measurements from Green et al. (2019) are based on stellar photometry from Pan-STARRS 1 and the Two Micron All Sky Survey, as well as parallaxes from *Gaia*. Here we report only  $E(B-V)$  for the full line of sight. We convert Bayestar reddening  $E$  to  $E(B-V)$  using the standard  $E(B-V) = 0.883E$  (Schlafly & Finkbeiner 2011; Green et al. 2019).

## 3. METHODS

In this work, we use absorption observations against background continuum sources, bright at both 1420 MHz and  $\sim 100$  GHz, to determine the physical properties of the atomic and molecular gas in five different directions. We use a standard approach, described here, to extract the absorption spectra and constrain the column densities.

If the observed flux density at frequency  $\nu$  of a background continuum source is  $S(\nu)$  and the continuum flux density (i.e., the flux density not modified by absorption) is  $S_0(\nu)$ , then the absorption spectrum is defined as

$$e^{-\tau(\nu)} = \frac{S(\nu)}{S_0(\nu)}. \quad (1)$$

To measure  $S_0(\nu)$  in our data, we fit a first-order polynomial to  $S(\nu)$  for channels with no absorption. The first-order polynomial removes potential structure in the continuum spectrum introduced by the spectral index (this approach was previously used by Rybarczyk et al. 2022 for the HCO<sup>+</sup> spectra in the direction of 3C111, 3C120, and 3C454.3). We note that Equation 1 assumes that either the continuum brightness temperature is much larger than the excitation temperature of the relevant transition, or that emission in that transition is spa-

tially extended such that it will be filtered out by the interferometer, or both.

These criteria should be met for all our observations, as the molecular lines have very low excitation temperatures (see discussion below) and we deliberately remove short baselines from the HI observations to prevent contamination from resolved emission. Moreover, if we remove the shortest baselines (we tested for baselines  $< 100$  m and  $< 200$  m) from our NOEMA and ALMA CO and HCO<sup>+</sup> observations, we find statistically insignificant changes in the channel-by-channel optical depths or integrated optical depth in all but one case. The only spectrum for which we detect significant changes in the optical depth when removing short baselines is the CO spectrum in the direction of 3C111, where we detect up to  $\sim 5\sigma$  changes in two channels. However, these are channels in the range where CO absorption is saturated, so the optical depth is already unconstrained (see discussion below). This is largely consistent with expectations — if we assume a CO excitation temperature of 4 K in the diffuse ISM (Luo et al. 2020), and a brightness temperature of CO emission of  $\sim 1$  K at small (sub-arcminute) scales (Liszt & Lucas 1998; see detailed maps in the directions of 3C454.3 and NRAO 530 in Liszt & Pety 2012), then in most cases, the potential CO emission, if it has not been filtered out by interferometer, would contribute no more than a few percent of the measured background brightness temperature at our current angular resolution. Thus, they have a negligible effect on the measured optical depths. The CO emission is significantly stronger in the direction of 3C111, though ( $\sim 4$  K, Liszt & Lucas 1998; see also the lower-resolution CO emission spectra in Figure 1). The same arguments hold for HCO<sup>+</sup>, but HCO<sup>+</sup> emission is often significantly weaker than CO emission (Lucas & Liszt 1996). And again, the potential contamination from emission will only align with denser regions where the HCO<sup>+</sup> absorption is particularly strong. In summary, contamination from emission will have a minimal impact on our measured optical depths in all but one case (and in that one case — the CO spectrum towards 3C111 — we do not report the optical depth at the contaminated velocity due to line saturation). In order to preserve the best noise possible, we therefore do include all baselines used by ALMA and NOEMA for CO, noting that an additional uncertainty of  $\sim \text{few}\%$  may result in regions of strong CO absorption.

Once we have extracted the absorption spectrum for a particular transition from upper state  $u$  to lower state

**Table 3.** Conversions from  $\int \tau dv$  to column density

$T_{\text{ex}}$	$N/\int \tau_{\text{CO}} dv$	$N/\int \tau_{\text{HCO}^+} dv$
K	$10^{15} \text{cm}^{-2}/\text{km s}^{-1}$	$10^{12} \text{cm}^{-2}/\text{km s}^{-1}$
$T_{\text{CMB}} = 2.725$	1.07	1.09
4.1	1.67	1.83
5	2.16	2.43
10	6.18	7.48

$l$ , at frequency  $\nu_0$ , we can solve for the column density

$$N = Q(T_{\text{ex}}) \frac{8\pi\nu^3}{c^3} \frac{1}{g_u A_{ul}} \left[ 1 - \exp\left(-\frac{h\nu_0}{kT_{\text{ex}}}\right) \right]^{-1} \int \tau(v) dv. \quad (2)$$

Here,  $g_u$  is the degeneracy of the upper energy state,  $A_{ul}$  is the Einstein  $A$  coefficient for the transition,  $T_{\text{ex}}$  is the excitation temperature, and  $Q(T_{\text{ex}})$  is the partition function. We have also expressed the optical depth in terms of velocity  $v$  rather than frequency in Equation 2.

Without absorption observations of higher-level rotational transitions, we cannot measure the excitation temperature of HCO<sup>+</sup> or CO directly. Previous measurements of the HCO<sup>+</sup> excitation temperature in the diffuse/translucent ISM have all been consistent with  $T_{\text{ex}} \approx T_{\text{CMB}} = 2.725$  K (2.7–3.0 K; Godard et al. 2010; Luo et al. 2020). Luo et al. (2020) specifically derived an excitation temperature  $T_{\text{ex}} = 2.7$  K for HCO<sup>+</sup> in the direction of 3C454.3. Meanwhile, Goldsmith (2013) measured CO excitation temperatures 2.7–13.6 K (with 63/64 measured excitation temperatures  $\leq 6.0$  K) from UV measurements in the direction of stars in the solar neighborhood, probing diffuse gas. Luo et al. (2020) measured the  $J=(1-0)$  and  $J=(2-1)$  transitions of CO in the direction of 3C454.3, deriving a CO excitation temperature  $T_{\text{ex}} = 4.1$  K. More generally, RADEX modeling of the CO  $J=(1-0)$  and  $J=(2-1)$  transitions toward four diffuse sightlines by Luo et al. (2023) yields excitation temperatures of  $\sim 3$ –4 K. These sub-thermal excitation temperatures should be appropriate for the majority of the CO detections in our sample.

In Table 3, we give the conversion between integrated optical depth and column density (Equation 2) for CO and HCO<sup>+</sup> for a range of values of  $T_{\text{ex}}$ . Throughout the rest of this work, we assume  $T_{\text{ex}} = T_{\text{CMB}}$  for HCO<sup>+</sup> for all directions. Because the CO excitation temperature is less tightly constrained in the diffuse ISM, we consider a range of possible CO excitation temperatures moving forward.

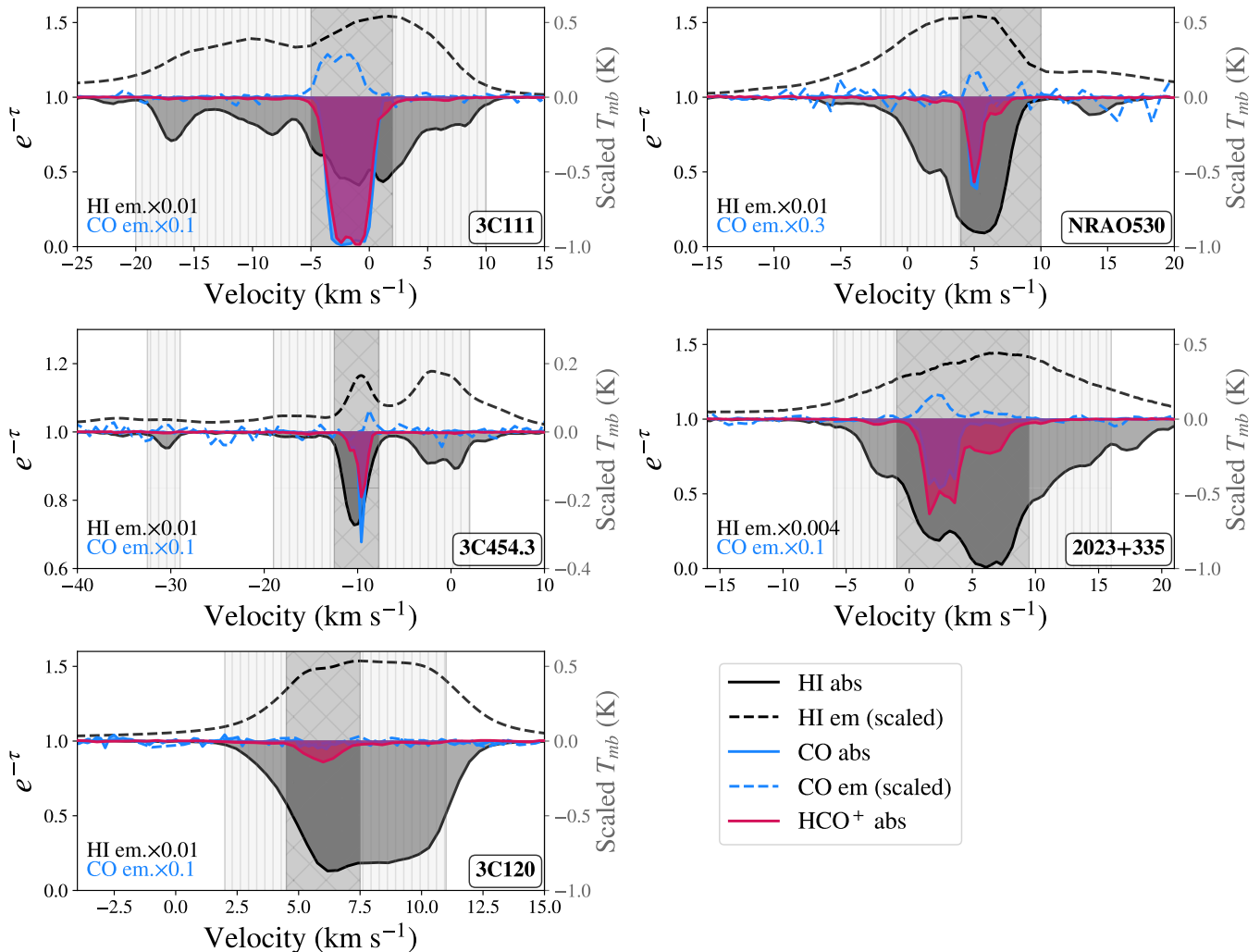


**Figure 1.** The absorption spectra,  $e^{-\tau}$ , of HI (filled black),  $\text{HCO}^+$  (filled pink), and CO (filled blue) in the direction of the five background sources listed in Table 2. Velocities where narrow  $\text{HCO}^+$  absorption is observed are highlighted in cross-hatched dark gray (see Figure 2, which highlights the broad, weak spectral features, difficult to see in these plots). Velocities where broad  $\text{HCO}^+$  absorption is observed are highlighted in vertically hatched light gray. HI emission (dashed black line) and CO emission (dashed blue line) are also shown for context; the right-hand  $y$ -axis shows the brightness temperature for HI and CO emission, scaled by the factors indicated in the bottom left corner of each plot.

Meanwhile, for HI, the excitation temperature (generally referred to as the “spin temperature,”  $T_s$ ) is much higher than  $T_{\text{CMB}}$ . In this work, we calculate spin temperatures using an isothermal approximation, which assigns a single spin temperature to the atomic gas in each velocity channel (essentially ignoring the blending of different components that may have differing  $T_s$ ). This is equal to  $T_s(v) = T_B(v)(1 - e^{-\tau(v)})^{-1}$ . The HI column densities are then calculated as  $N(\text{HI}) = 1.823 \times 10^{18} \times \int T_s(v)\tau(v)dv$ . In the future, we will consider HI column densities for discrete HI clouds along each line of sight (see Section 5.2.2), but the isothermal approximation to measuring the integrated column den-

sity agrees reasonably well with this more sophisticated approach in most cases (e.g., Murray et al. 2018).

#### 4. RESULTS

We detect absorption from CO,  $\text{HCO}^+$ , and HI toward all five background radio continuum sources. In Figures 1 and 2, we show the absorption spectra,  $e^{-\tau(v)}$ , for CO (blue),  $\text{HCO}^+$  (pink), and HI (black) in all five directions. Figure 1 shows the entire spectra, as well as the HI and CO emission spectra in the same directions (dotted lines) for context, while Figure 2 focuses on the shallow, broad  $\text{HCO}^+$  absorption discussed by Liszt & Lucas (2000) and Rybarczyk et al. (2022, 2023).

In this work, we are focused primarily on understanding the origin and physical properties of the gas traced

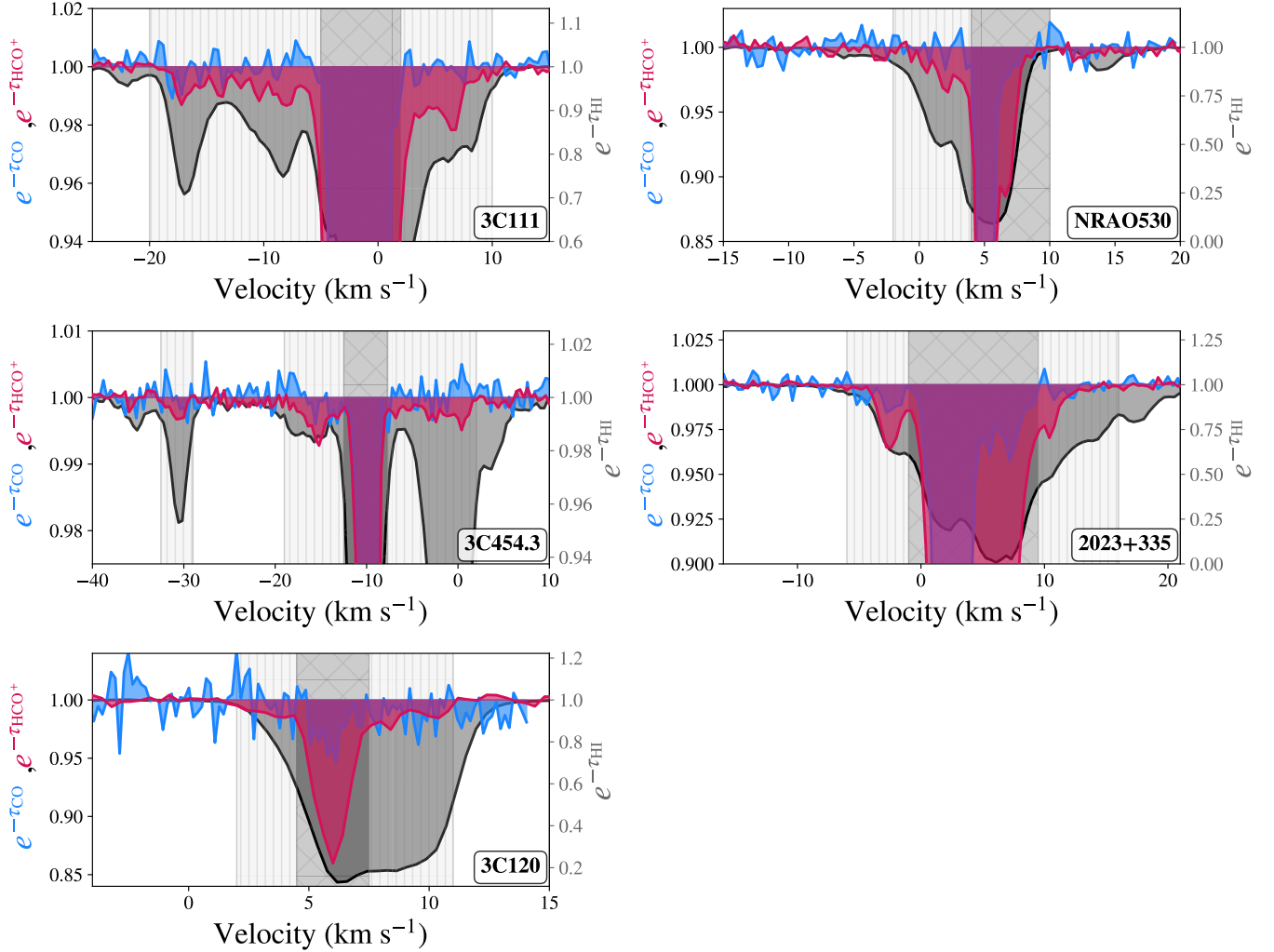


**Figure 2.** Same as Figure 1, but with restricted  $y$ -axis ranges to highlight the broad  $\text{HCO}^+$  absorption component. The left  $y$ -axis shows  $e^{-\tau}$  for CO and  $\text{HCO}^+$ , while the right axis shows  $e^{-\tau}$  for HI. We do not show the HI and CO emission here.

by broad  $\text{HCO}^+$  absorption. We must therefore explicitly define what is meant by broad versus narrow. In previous work, “narrow” has referred to spectral intervals where the strongest  $\text{HCO}^+$  absorption is observed (on a sightline-by-sightline basis), confined to a relatively narrow range of velocities ( $\sim$  few  $\text{km s}^{-1}$ ) and comprising one or a few narrow peaks. Conversely, “broad” has referred to spectral intervals where the  $\text{HCO}^+$  absorption is notably weaker, typically extending several  $\text{km s}^{-1}$  to one or both sides of the narrow absorption (Liszt & Lucas 2000; Rybarczyk et al. 2022). Rybarczyk et al. 2022 earlier defined the “broad” and “narrow” regions for 3C111, 3C120, and 3C454.3 based solely on the  $\text{HCO}^+$  absorption profiles; for consistency, we adopt their bounds for these sightlines. For our other two sightlines, we adopt a similar approach to defining broad and narrow absorption. Namely, we use “narrow” (on a sightline-by-sightline basis) to refer to spectral inter-

vals where the strongest  $\text{HCO}^+$  absorption is observed (typically,  $\tau_{\text{HCO}^+} \gtrsim 0.1$ ), confined to a relatively narrow range of velocities ( $\sim$  few  $\text{km s}^{-1}$ ) comprising one or a few narrow peaks. Regions of narrow absorption are highlighted in cross-hatched dark gray in Figures 1 and 2. Meanwhile, we use “broad” to refer to spectral intervals where the  $\text{HCO}^+$  absorption is weaker and extends several  $\text{km s}^{-1}$  beyond where the narrow absorption lines are observed. The broad absorption does not necessarily comprise absorbing components with particularly broad linewidths, but contributes to the overall breadth of the  $\text{HCO}^+$  absorption in a given direction. Regions of narrow absorption are highlighted in cross-hatched dark gray in Figures 1 and 2, whereas regions of broad absorption are highlighted in vertically-hatched light gray. Median signal-to-noise values for the broad spectral regions are  $\sim 2.5$ –7.

We note that while we adopt this categorization for consistency with the existing literature (Liszt & Lucas 2000; Rybarczyk et al. 2022), we do not mean to automatically imply physical or chemical differences. Later we discuss how both the broad and narrow absorption features fit into our understanding of the diffuse ISM.

#### 4.1. Integrated $\text{HCO}^+$ and CO optical depths

In Table 4, we list the velocity bounds for each of the broad and narrow regions in Figures 1 and 2, as well as their integrated CO and  $\text{HCO}^+$  optical depths. Narrow  $\text{HCO}^+$  absorption is detected in all directions. The narrow  $\text{HCO}^+$  absorption is associated with the strongest HI absorption in each direction and is coincident with narrow CO absorption in all cases. The broad  $\text{HCO}^+$  component extends across nearly all velocities where HI is detected in absorption, rather than just the optically thickest HI associated with the strong, narrow molecular features. Toward J2023+335, we detect some CO associated with broad  $\text{HCO}^+$  absorption, but most of the broad  $\text{HCO}^+$  absorption is CO-dark at the sensitivity achieved here (Table 2).

In Figure 3, we show the integrated CO optical depth versus the integrated  $\text{HCO}^+$  optical depth for all regions listed in Table 4. Regions with narrow  $\text{HCO}^+$  absorption are shown as orange squares and regions with broad  $\text{HCO}^+$  absorption are shown as purple circles. There is a clear separation in this space, with the narrow absorption having systematically higher  $\int \tau_{\text{CO}} dv$  and  $\int \tau_{\text{HCO}^+} dv$  (in the latter case, this is expected from the definition of narrow absorption, as discussed above). CO is detected in all five regions with narrow  $\text{HCO}^+$  absorption, but in only one of the 10 regions with broad  $\text{HCO}^+$  absorption (J2023+335). It is notable here that the narrow absorption toward 3C120 (the orange point with the lowest  $\int \tau_{\text{CO}} dv$ ) lies at the interface of the broad and narrow regimes on this plot, perhaps suggesting that it is tracing a more diffuse environment than the other narrow components.

From Figure 3, we find an approximate threshold of  $\int \tau_{\text{HCO}^+} \sim 0.2 \text{ km s}^{-1}$  below which most of the diffuse molecular gas is CO-dark.

If we assume  $N(\text{HCO}^+)/N(\text{H}_2) = 3 \times 10^{-9}$  (Liszt & Gerin 2023b) and an  $\text{HCO}^+$  excitation temperature 2.725 K (which is well justified; see Section 3), then this implies that the diffuse molecular gas in our sample is mostly CO-dark below a threshold of  $N(\text{H}_2) \sim 7 \times 10^{19} \text{ cm}^{-2}$ . The only exception is the detection of CO toward the broad component of J2023+335, associ-

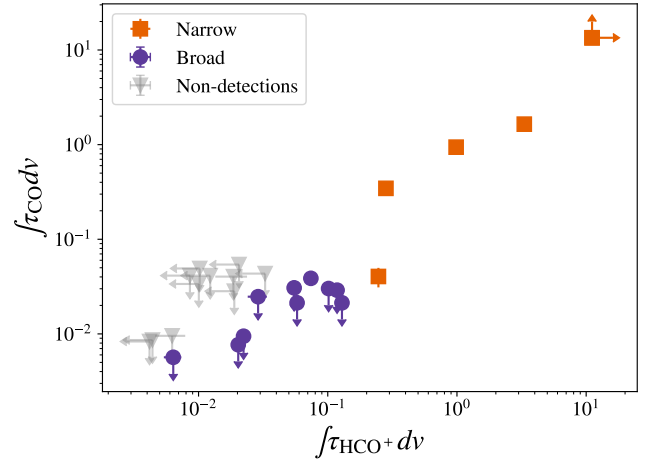


**Figure 3.** The integrated CO optical depth versus the integrated  $\text{HCO}^+$  optical depth for different velocity intervals (listed in Table 4). Results for regions with broad  $\text{HCO}^+$  absorption are shown as purple circles. Results for regions with narrow  $\text{HCO}^+$  absorption are shown as orange squares. For non-detections,  $3\sigma$  upper limits are shown as semi-transparent gray triangles. For points without clear error bars, the uncertainties are smaller than the sizes of the points.

ated with an  $\text{HCO}^+$  column density  $\sim 8 \times 10^{10} \text{ cm}^{-2}$ , implying an  $\text{H}_2$  column density  $\sim 3 \times 10^{19} \text{ cm}^{-2}$ .

On a sightline-by-sightline basis, we estimate that the fraction of the molecular hydrogen that is CO-dark is between 3% and 20% (here taken as the fraction of the  $\text{HCO}^+$  column density in channels with no CO absorption at a level of  $3\sigma$ ). Naturally, the CO-dark fraction will vary with environment; as expected, we find the highest CO-dark fractions towards sightlines with lower molecular column densities.

#### 4.2. The CO abundance

In Figure 4, we show the implied CO abundance relative to  $\text{H}_2$  (top panel) and relative to all hydrogen nuclei ( $\text{HI}+\text{H}_2$ ; bottom panel). Here,  $N(\text{H}_2)$  is derived directly from  $N(\text{HCO}^+)$  using the assumed abundance of  $3 \times 10^{-9}$ , and  $N(\text{HI})$  is derived from emission and absorption as described in Section 3. We note that results for the narrow absorption toward 3C111 are not included — because both CO and  $\text{HCO}^+$  are saturated, the CO abundance is unconstrained. Opaque points show the results for a CO excitation temperature of  $T_{\text{CMB}}$ ; semi-transparent points show the results for a CO excitation temperature of 6 K. Based on previous observations at similar column densities in the diffuse ISM (e.g., Goldsmith 2013; Luo et al. 2020, 2023), true values likely lie between these two limits (see Section 3).

The implied CO abundances relative to  $\text{H}_2$  are a few  $\times 10^{-7}$  to a few  $\times 10^{-6}$  for regions traced by narrow

**Table 4.** The integrated CO and HCO<sup>+</sup> optical depths and their ratios for each region outlined in Figure 2.

Sightline	Type	Velocity interval	$\int \tau_{\text{HCO}^+} dv$	$\int \tau_{\text{CO}} dv$	$\frac{\int \tau_{\text{HCO}^+} dv}{\int \tau_{\text{CO}} dv}$
		km s <sup>-1</sup>	km s <sup>-1</sup>	km s <sup>-1</sup>	
3C111	none	[-40.0, -20.0)	< 0.010	< 0.034	...
	broad	[-20.0, -5.0)	0.118 ± 0.003	< 0.029	> 4.073
	narrow	[-5.0, 2.0)	11.108 <sup>a</sup>	13.459 <sup>a</sup>	0.825 <sup>a</sup>
	broad	[2.0, 10.0)	0.129 ± 0.002	< 0.021	> 6.045
	none	[10.0, 40.0)	< 0.012	< 0.041	...
NRAO530	none	[-20.0, -2.0)	< 0.021	< 0.054	...
	broad	[-2.0, 4.0)	0.102 ± 0.004	< 0.030	> 3.366
	narrow	[4.0, 10.0)	0.985 ± 0.005	0.941 ± 0.010	1.047 ± 0.013
	none	[10.0, 20.0)	0.019 ± 0.005	< 0.040	> 0.462
J2023+335	none	[-40.0, -6.0)	< 0.010	< 0.049	...
	broad	[-6.0, -1.0)	0.074 ± 0.001	0.039 ± 0.006	1.915 ± 0.307
	narrow	[-1.0, 9.5)	3.319 ± 0.003	1.646 ± 0.009	2.016 ± 0.011
	broad	[9.5, 16.0)	0.058 ± 0.001	< 0.021	> 2.714
	none	[16.0, 40.0)	< 0.009	< 0.041	...
3C454.3	none	[-40.0, -32.5)	< 0.004	< 0.008	...
	broad	[-32.5, -29.0)	0.006 ± 0.001	< 0.006	> 1.126
	none	[-29.0, -19.0)	0.006 ± 0.002	< 0.010	> 0.655
	broad	[-19.0, -12.5)	0.020 ± 0.001	< 0.008	> 2.640
	narrow	[-12.5, -7.75)	0.282 ± 0.001	0.345 ± 0.002	0.817 ± 0.006
	broad	[-7.75, 2.0)	0.022 ± 0.002	< 0.009	> 2.359
	none	[2.0, 10.0)	< 0.004	< 0.009	...
3C120	none	[-10.0, 2.0)	< 0.033	< 0.043	...
	broad	[2.0, 4.5)	0.029 ± 0.005	< 0.025	> 1.169
	narrow	[4.5, 7.5)	0.247 ± 0.005	0.040 ± 0.009	6.098 ± 1.427
	broad	[7.5, 11.0)	0.055 ± 0.006	< 0.031	> 1.791
	none	[11.0, 15.0)	< 0.019	< 0.028	...

<sup>a</sup>Because of saturation for both CO and HCO<sup>+</sup> in the direction of 3C111, the integrated optical depths are both lower limits, so the ratio is not constrained.

HCO<sup>+</sup> absorption and  $\lesssim$  a few  $\times 10^{-6}$  (upper limits) for regions traced by broad HCO<sup>+</sup> absorption. Similarly, the implied CO abundances relative to all hydrogen nuclei are few  $\times 10^{-8}$  to few  $\times 10^{-6}$  for regions traced by narrow HCO<sup>+</sup> absorption and  $\lesssim$  few  $\times 10^{-7}$  (upper limits) for regions traced by broad HCO<sup>+</sup> absorption. As in Figure 3, we find that the narrow absorption toward 3C120 (the orange point with the lowest abundance — in both panels — in Figure 4) falls in a similar area of parameter space to the broad absorption in other directions. More generally, our measurements are not sufficient to conclude whether the CO abundance relative to H<sub>2</sub> is systematically lower for gas traced by broad absorption. We note that the abundances relative to

all hydrogen nuclei (bottom panel of Figure 4) appear systematically higher for regions traced by narrow absorption (excluding the direction of 3C120), but this is expected given the similar abundances (or limits) relative to H<sub>2</sub> (top panel of Figure 4), combined with the lower molecular fractions for gas traced by broad absorption (see Section 4.3 below).

### 4.3. Comparing HI and diffuse molecular gas properties

#### 4.3.1. The CNM fraction and molecular gas fraction

Rybarczyk et al. (2022) previously showed that the HI associated with broad HCO<sup>+</sup> absorption had a lower CNM fraction than that associated with narrow

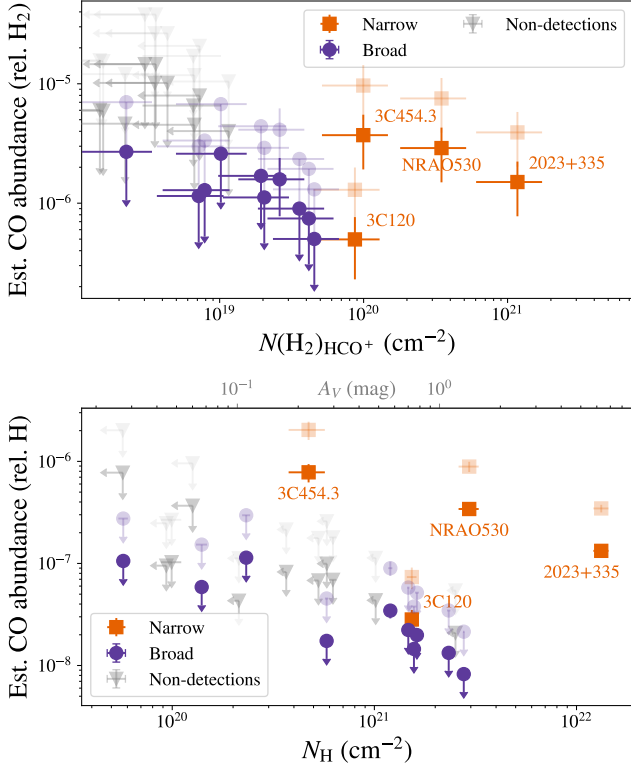


**Figure 4.** *Top:* the implied CO abundance relative to  $\text{H}_2$  versus the  $\text{H}_2$  column density (derived from the  $\text{HCO}^+$  column density) for all regions listed in Table 4. *Bottom:* the implied CO abundance relative to the total hydrogen column density versus the total column density,  $N_{\text{H}}$  (derived from the  $\text{HCO}^+$  column density and the HI column density) for all regions listed in Table 4. We also show  $A_V$  in the bottom panel, where we convert to  $A_V$  from  $N_{\text{H}}$  assuming  $A_V = N_{\text{H}}/2.1 \times 10^{21} \text{ mag/cm}^{-2}$  (Güver & Özel 2009; Zhu et al. 2017). In both plots, the results for regions with narrow absorption are shown with orange squares (labeled for each sightline) and the results for regions with broad absorption are shown with purple circles. Results for regions with neither  $\text{HCO}^+$  nor CO detections are shown as gray triangles. The CO excitation temperature is unknown; solid points show results for a CO excitation temperature of 2.725 K and semi-transparent points show results for a CO excitation temperature of 6 K.

$\text{HCO}^+$  absorption. Here we perform a similar analysis for our current sample, by comparing the integrated  $\text{HCO}^+$  optical depth and the HI optical-depth-weighted mean spin temperature,

$$\langle T_s \rangle = \frac{\int \tau(v) T_{\text{B}}(v) / (1 - e^{-\tau(v)}) dv}{\int \tau(v) dv}. \quad (3)$$

This quantity is not, in general, the actual physical temperature of the gas, as there may be multiple structures with different temperatures blended in velocity space. Instead,  $\langle T_s \rangle$  is a proxy for the frac-

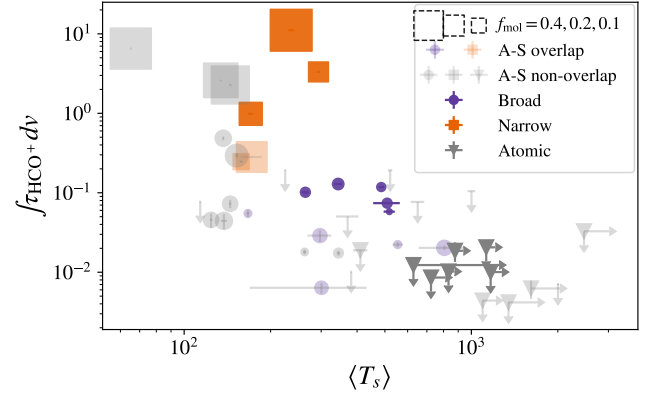


**Figure 5.** The integrated  $\text{HCO}^+$  optical depth versus  $\langle T_s \rangle$  (Equation 3). Results for regions with narrow  $\text{HCO}^+$  absorption are shown as squares. Results for regions with broad  $\text{HCO}^+$  absorption are shown as circles. Results for regions where only atomic gas is detected in absorption are shown as triangles. New results from this work are plotted in opaque orange (for narrow absorption regions), purple (for broad absorption regions) and solid gray (for regions with no molecular absorption) markers. Data from the ALMA-SPONGE project (Rybarczyk et al. 2022) toward the sightlines discussed here are shown in the same color scheme with semi-transparent markers (labeled “A-S overlap”). Data from Rybarczyk et al. (2022) in other directions are shown in semi-transparent gray (labeled “A-S non-overlap”). Markers are sized according to the molecular fraction,  $f_{\text{mol}}$  (the legend shows marker sizes for  $f_{\text{mol}} = 0.4, 0.2, \text{ and } 0.1$  for reference).

tion of HI in the CNM, being inversely proportional to  $f_{\text{CNM}} = N(\text{HI}_{\text{CNM}})/N(\text{HI})$  (Kim et al. 2014). Figure 5 shows the integrated  $\text{HCO}^+$  optical depth versus  $\langle T_s \rangle$  for regions with narrow  $\text{HCO}^+$  absorption (orange squares), broad  $\text{HCO}^+$  absorption (purple circles), and with no  $\text{HCO}^+$  absorption (triangles). Results from Rybarczyk et al. (2022) are also overplotted.<sup>5</sup> Points are sized according to the molecular fraction,  $f_{\text{mol}} = 2N(\text{H}_2)/[N(\text{HI}) + 2N(\text{H}_2)]$ .

As in Rybarczyk et al. (2022), we find that the integrated  $\text{HCO}^+$  optical depth — and therefore,  $N(\text{HCO}^+)$  and, by extension,  $N(\text{H}_2)$  — decreases with increasing  $\langle T_s \rangle$ . In particular, broad (mostly CO-dark)  $\text{HCO}^+$  absorption is found in regions with systematically higher  $\langle T_s \rangle$  (and therefore lower  $f_{\text{CNM}}$ ) than regions with nar-

<sup>5</sup> Rybarczyk et al. (2022) considered HI and  $\text{HCO}^+$  toward 3C111, 3C120, and 3C454.3 (including data from Luo et al. 2020), as well as four additional sightlines. In Figure 5, the results for 3C120 and 3C454.3 are plotted with semi-transparent colored markers to indicate the overlap with this work, whereas the results for 3C111 are plotted as opaque points, since we re-calculated  $\int \tau_{\text{HCO}^+} dv$  for the new, more sensitive spectra presented here (see Section 2.1). We also note that Rybarczyk et al. (2022) did not observe CO absorption in any direction.

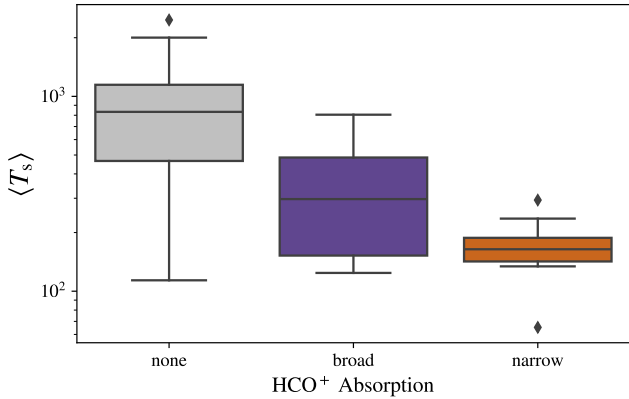


**Figure 6.** Box plot of  $\langle T_s \rangle$  (Equation 3) for regions with narrow  $\text{HCO}^+$  absorption (orange, rightmost), broad  $\text{HCO}^+$  absorption (purple, middle), and no  $\text{HCO}^+$  absorption (gray, leftmost). The boundaries of the box are drawn at the first and third quartiles, with the median indicated by a horizontal line. The “whiskers” show the extent of the data, with outliers shown as diamond points.

row  $\text{HCO}^+$  (and narrow CO absorption). This is illustrated more clearly in the box plot shown in Figure 6. These results are consistent with previous work that has shown that denser, CO-bright molecular gas is found preferentially in directions with relatively high CNM fraction (e.g., Stanimirović et al. 2014; Nguyen et al. 2019; McClure-Griffiths et al. 2023; Park et al. 2023), and they reinforce the conclusion from Rybarczyk et al. (2022) that the broad  $\text{HCO}^+$  absorption is tracing gas with systematically different physical properties (though Rybarczyk et al. 2022 only observed CO emission, not CO absorption).

We estimate  $f_{\text{CNM}}$  from  $\langle T_s \rangle$  using Equation 18 of Kim et al. (2014) (where we assume a typical CNM cloud temperature between 50 K and 150 K and a typical WNM cloud temperature between 1000 K and 6000 K; e.g., Murray et al. 2021). Based on the data in Figure 6, narrow  $\text{HCO}^+$  absorption (associated with narrow CO absorption and, in some cases, CO emission) is detected where  $f_{\text{CNM}} = 0.64^{+0.28}_{-0.31}$  while broad (mostly CO-dark)  $\text{HCO}^+$  absorption is detected where  $f_{\text{CNM}} = 0.38^{+0.28}_{-0.27}$  (upper and lower bounds indicate the 15.9 and 84.1 percentiles).

It is also clear from Figure 5 that the *molecular* fraction is systematically lower in regions with broad  $\text{HCO}^+$  absorption. For the gas traced by narrow  $\text{HCO}^+$  absorption,  $f_{\text{mol}} = 0.60^{+0.24}_{-0.18}$ , while for broad absorption,  $f_{\text{mol}} = 0.09^{+0.06}_{-0.03}$ . In other words, not only is the total amount of  $\text{H}_2$  lower in these more diffuse regions, but the fraction of hydrogen in  $\text{H}_2$  is also lower. This complements previous work showing that the CO emis-

sion detectable in existing surveys arises largely from gas with a high molecular fraction ( $f_{\text{mol}} \gtrsim 0.5$ ; Liszt 2017).

#### 4.3.2. The HI conditions necessary for the formation of molecular gas in the diffuse ISM

The association of molecular gas with the CNM is well-demonstrated observationally (e.g., Stanimirović et al. 2014), and well-understood theoretically (e.g., Goldsmith et al. 2007). In particular, molecular gas has been shown to exist only in directions where the HI optical depth is  $\gtrsim 0.1$  and the HI spin temperature is  $\lesssim 150$  K (Rybarczyk et al. 2022; Park et al. 2023; Hafner et al. 2023). However, as discussed explicitly by Rybarczyk et al. (2022), this previous work focused exclusively on narrow absorption — a fact that is also evident from a qualitative assessment of the published spectra.

Here, despite this difference, our results are largely consistent with previous work, in that we find that most  $\text{HCO}^+$  is detected where  $\tau_{\text{HI}} \gtrsim 0.1$ , including for the broad  $\text{HCO}^+$  absorption. However, while studies focusing on the equivalent of our narrow components find these thresholds to be a necessary but not sufficient condition for the presence of molecules (Hafner et al. 2023; Park et al. 2023), our detection rates are far higher — close to 100% for  $\tau_{\text{HI}} > 0.1$ . Furthermore, in the case of 3C454.3, we find two  $\text{HCO}^+$  components coincident with peak HI optical depths of around  $\tau \approx 0.01\text{--}0.05$  (near  $v = -16$  km s $^{-1}$  and  $v = -31$  km s $^{-1}$ ).

#### 4.3.3. Comment on velocity-resolved properties

While we have focused on the integrated properties of  $\text{HCO}^+$ , CO, and HI, it is clear from Figures 1 and 2 that both broad and narrow regions likely contain multiple absorbing components, so the integrated quantities represent weighted averages over multiple clouds. To look at the atomic and molecular gas more locally, we show the differential column density in each velocity bin in Figure 7 (here all spectra have been smoothed to 1 km s $^{-1}$  resolution for clarity). We further show the estimated molecular fraction in each velocity bin using blue scatter points. It is clear from Figure 7 that the trends reported earlier also hold on a channel-by-channel basis. Typical column densities for the broad components are systematically lower than those for the narrow components, and the same is true of the molecular fraction. In future work, we will consider a full spectral decomposition to extend this analysis to a cloud-by-cloud basis (see Section 5.2.2).

## 5. DISCUSSION

Using observations of CO absorption in directions where broad  $\text{HCO}^+$  absorption was previously detected,

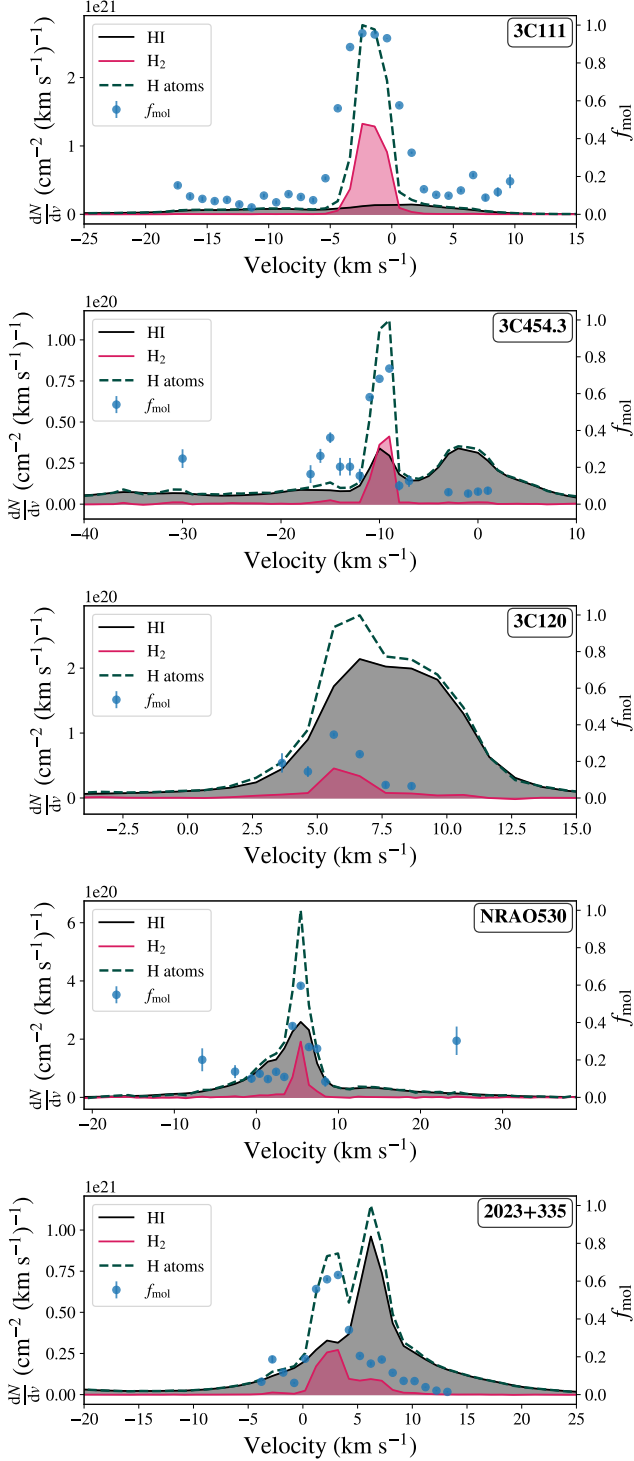


**Figure 7.** Spectra showing the differential column density in each velocity channel contributed by H<sub>2</sub> (pink, calculated from HCO<sup>+</sup>), HI (black, using an isothermal approximation in each channel), and the total hydrogen column (dashed dark green, using the sum of HI and 2 × H<sub>2</sub>). The molecular fraction in each velocity bin where HCO<sup>+</sup> is detected is shown as a blue scatter point. Spectra have been smoothed to 1  $\text{km s}^{-1}$  resolution.

we have shown that the broad HCO<sup>+</sup> absorption signature first identified by Liszt & Lucas (2000) and recently characterized by Rybarczyk et al. (2022) is indeed mostly CO-dark\* and CO-dark (Figures 1 and 2). The CO absorption observations were necessary to make this comparison, since (1) they probe roughly the same spatial scales as previous HCO<sup>+</sup> absorption observations, and (2) they are more sensitive to low column density CO than emission observations in these directions (our absorption observations have roughly an order of magnitude better column density sensitivity to CO for a given CO abundance compared to the emission data from Dame & Thaddeus 2022). While we detect CO in all directions, nearly all of the CO absorption is associated with strong, narrow HCO<sup>+</sup> absorption.

### 5.1. Why is the broad component CO-dark?

#### 5.1.1. The CO abundance and its implications

In Section 4.2, we measure CO abundances (and upper limits) in the diffuse molecular gas probed by our observations (Figure 4), finding values (relative to H<sub>2</sub>) of  $\lesssim 10^{-5}$ . This is low compared to those expected in classic CO-bright molecular clouds  $\sim 10^{-4}$  (e.g., Federman et al. 1990; Liu et al. 2013). However, even for our narrow absorption lines, the gas we are probing is diffuse in almost all cases, as we will discuss presently. The two exceptions are the saturated absorption in 3C111, and the  $\sim 2.5 \text{ km s}^{-1}$  narrow absorption component in J2023+335. The former is associated with the California molecular cloud, shows correspondingly bright CO emission ( $\sim 3.3 \text{ K}$ ) in Dame & Thaddeus (2022), and is in any case excluded from our analysis because of line saturation. The latter is a low Galactic Latitude sightline ( $b = -2.36^\circ$ ) passing through disk molecular gas, with a CO brightness temperature of  $\sim 1.9 \text{ K}$  (Dame & Thaddeus 2022). We will discuss this sightline further below.

For all components, the abundances (as well as the upper limits) that we measure are consistent with the expected values from the literature for diffuse sightlines. For example, the top panel of Figure 4 is entirely consistent with Figure 6 of Sheffer et al. (2008), whose direct observations of CO (optical) and H<sub>2</sub> (UV) indicated CO abundances relative to H<sub>2</sub> of  $\sim 10^{-7}$ – $10^{-5}$  for  $N(\text{H}_2) \sim 10^{19} \text{ cm}^{-3}$ – $10^{21} \text{ cm}^{-3}$  — albeit on a sightline-integrated basis. Meanwhile, it is understood that the CO abundance falls off sharply for  $A_V \lesssim 1 \text{ mag}$  (e.g., Wolfire et al. 2010). The bottom panel of Figure 4 indicates that all of our plotted regions indeed have  $A_V \lesssim 1 \text{ mag}$  (where  $A_V \approx N_{\text{H}}/2.1 \times 10^{21} \text{ mag/cm}^{-2}$ , e.g., Güver & Özel 2009; Zhu et al. 2017), except for the narrow absorption in the direction of J2023+335

(the rightmost point on the plot). The CO abundances and upper limits that we measure relative to all hydrogen nuclei are consistent with model expectations for  $0.1 \text{ mag} \lesssim A_V \lesssim 1 \text{ mag}$  from [Wolfire et al. \(2010\)](#), who modeled CO-dark gas using a 1D photodissociation region with uniform radiation field using code from [Kaufman et al. \(2006\)](#) adapted to better account for CO chemistry. There, while their CO abundances (relative to all hydrogen nuclei) span over five orders of magnitude in this  $A_V$  range, they do not exceed  $\sim 10^{-5}$ .

For the discrepant component — the J2023+335 narrow absorption — the implied  $A_V > 1 \text{ mag}$  and the detection of CO emission might suggest that this component arises from a classic CO-bright molecular cloud, making the low abundance we obtain here puzzling. However, there are several mitigating factors. The first is that the [Dame & Thaddeus \(2022\)](#) CO emission data is of very coarse resolution and undersampled, meaning that it may not well represent the pencil beam absorption measurement from which our abundance is derived. The second is that the subthermal excitation temperatures we assume in this work may not be appropriate for this component (if it is indeed associated with emitting gas), meaning that the CO column (and hence the abundance) could be underestimated by a factor of a few. Finally the  $A_V$  we estimate here includes a significant contribution from the velocity-integrated HI column within with our broad and narrow velocity ranges. In reality it is clear from the complex, blended HI absorption spectra that multiple components are overlapping in velocity along these sightlines, only some of which may be spatially co-located with molecular gas. As a result, the  $A_V$  is almost certainly overestimated to some degree (in all components). Decomposing the atomic and molecular absorption spectra in future work (see [Section 5.2.2](#)) will be important for placing tighter constraints on the CO abundance for individual structures along the line of sight.

Figure 8 shows the sensitivity required to detect CO in absorption for a range of  $\text{H}_2$  column densities and CO abundances appropriate to the diffuse ISM. The approximate sensitivity achieved in the present work is indicated with a semi-transparent window (calculated for  $\sigma_\tau \sim 3 \times 10^{-3}$  and assuming a full-width at half-maximum between  $1 \text{ km s}^{-1}$  and  $4 \text{ km s}^{-1}$  and excitation temperature  $2.725 \text{ K} \leq T_{\text{ex}} \leq 6 \text{ K}$ ; [Liszt & Lucas 1998](#); [Luo et al. 2020](#)), consistent with the detections shown in Figure 4. Based on these model predictions for the CO abundance ([Wolfire et al. 2010](#)), and the optical depth sensitivities achievable with current radio observatories, it seems implausible to expect to detect CO in absorp-

tion for  $N(\text{H}_2) \lesssim \text{few} \times 10^{19} \text{ cm}^{-2}$ . This is consistent with our observational results.

While we are focused on CO absorption here, we note that for the  $\text{H}_2$  column densities ( $\lesssim \text{few} \times 10^{19} \text{ cm}^{-2}$ ) and CO abundances ( $< 10^{-5}$ ) associated with the broad component (Figure 4), the sensitivity needed to detect CO in emission is  $\sigma_{W_{\text{CO}}} \lesssim 10^{-2} \text{ K km s}^{-1}$  (see, e.g., Equation 18 of [Bolatto et al. 2013](#)). This is below the detection thresholds of even the most sensitive CO emission observations (e.g., [Li et al. 2018](#)). Indeed, we detect CO emission (Figure 1) only for the components with  $N(\text{H}_2) > \text{few} \times 10^{20} \text{ cm}^{-2}$ . This is consistent with theoretical expectations given the column densities and abundances in Figure 4 ( $W_{\text{CO}} \sim 0.2\text{--}3 \text{ K km s}^{-1}$ ; e.g., [Bolatto et al. 2013](#), and references therein).

To summarize, in the diffuse molecular sight lines observed here, the low CO abundances combined with intrinsically low molecular column densities can fully explain why CO is not generally detected with the broad  $\text{HCO}^+$  components. Similarly, we need not invoke higher CO abundances in the narrow  $\text{HCO}^+$  components to explain their detection in CO — this can be entirely explained by higher  $N(\text{H}_2)$ . CO in emission can be observed in these narrow and moderately diffuse components, despite CO abundances below the canonical  $10^{-4}$ .

### 5.1.2. The origin of the broad and narrow absorption

From Figure 3 we see that gas is CO-dark in our data where  $\int \tau_{\text{HCO}^+} dv \lesssim 0.2 \text{ K km s}^{-1}$ , corresponding to  $\text{H}_2$  column densities  $\lesssim \text{few} \times 10^{19} \text{ cm}^{-2}$  (as discussed above). The components we identify as narrow are, by definition, those with the highest peak  $\text{HCO}^+$  optical depths along the line of sight ( $\tau_{\text{HCO}^+} > 0.05$ ), and are therefore more likely to meet this threshold for CO detection. This fact remains true even if the CO abundance is the same for gas traced by broad and narrow absorption (a scenario that is not ruled out by the upper limits in Figure 4), because the narrow components are simply where sufficient molecular column has been accumulated to render CO detectable. Indeed, in Figure 7, we show that all regions identified as narrow are associated with the highest column densities and molecular fractions in each direction.

The picture then is one in which the distinction between *broad* and *narrow* absorption in diffuse molecular gas (which we have essentially adopted from previous work, e.g., [Liszt & Lucas 2000](#); [Rybarczyk et al. 2022](#)) is primarily one of molecular ( $\text{H}_2$ ) column density. Along any line of sight, higher column density, better-shielded gas with higher molecular fraction — and hence sufficient molecular column to be CO-bright (or at least

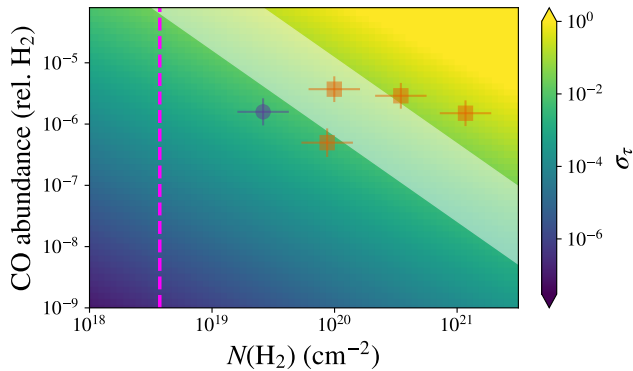


**Figure 8.** The optical depth sensitivity (color map) required to detect CO at  $3\sigma$  for a given  $\text{H}_2$  column density ( $x$ -axis) and CO abundance ( $y$ -axis). The semi-transparent white window shows the theoretical detectability limit for a CO optical depth sensitivity  $\sim 0.003$  (typical of what we obtain here; see Table 2) and a range of full-widths at half-maximum between  $1 \text{ km s}^{-1}$  and  $4 \text{ km s}^{-1}$  (Liszt & Lucas 1998; Luo et al. 2020) and  $2.725 \text{ K} \leq T_{\text{ex}} \leq 6 \text{ K}$ . The vertical dashed magenta line shows the  $\text{H}_2$  sensitivity limit for an  $\text{HCO}^+$  optical depth sensitivity of 0.002 (see Table 4). CO abundances measured here are shown as semi-transparent points (with the same styles and coloring as in Figure 4, but with non-detections removed). These points are all consistent with the theoretical detectability limit within  $< 2\sigma$ .

not CO-dark) — will tend to be spatially localized, and hence narrowly confined in velocity. Cold gas at intermediate column densities and lower molecular fraction similarly comprises multiple velocity components, but spread over a wider range of velocities. This gas is also partially molecular, but at a lower level, accumulating sufficient column density to be detectable in  $\text{HCO}^+$  but not in CO.

In most cases, it seems clear that the breadth of the broad  $\text{HCO}^+$  absorption is essentially set by the velocity distribution of the cold gas along the sightline — the faint  $\text{HCO}^+$  absorption traces nearly all velocities where we see HI absorption. In fact, in some cases (3C111, 3C454.3), our spectra show that the broad  $\text{HCO}^+$  absorption clearly comprises multiple discrete components with narrow linewidths, many of which are well-aligned with peaks in the HI absorption spectra (see Section 5.2.2).

## 5.2. Physical properties of diffuse molecular gas

### 5.2.1. Connection to multiphase HI

Fundamentally, we are interested in the detection of CO-dark (and CO-dark\*) diffuse gas not as an end in itself, but rather as a valuable probe of the physics and chemistry of the diffuse ISM. The multi-wavelength observations presented here have constrained some of the

physical conditions of the diffuse CO-dark(\*) gas, which is effectively traced by broad  $\text{HCO}^+$  absorption.

In Section 4, we show that narrow absorption features (which are not CO-dark, and in some cases are CO-bright) generally align with the optically thickest HI (Figure 1) and the highest total column density (Figure 7) in each direction. Both the CNM fraction and the molecular fraction are relatively high in these environments (Figure 7), despite still being diffuse ( $A_V \lesssim 1 \text{ mag}$ ) in most cases.

Meanwhile, the broad (mostly CO-dark)  $\text{HCO}^+$  absorption is associated with lower HI optical depths (Figures 1 and 2) and lower column density gas (Figure 7). In at least one case (3C454.3), we detect  $\text{HCO}^+$  at velocities where the peak HI optical depth is  $\tau \approx 0.01$ – $0.05$ , a factor of 2–10 lower than previously reported as an empirical threshold for the formation and survival of molecular gas ( $\tau \gtrsim 0.1$ ; e.g., Nguyen et al. 2019; Rybarczyk et al. 2022; Park et al. 2023; Hafner et al. 2023). In these environments, the CNM fraction and molecular fraction are both relatively low (Figures 6 and 7). The broad  $\text{HCO}^+$  absorption signature therefore traces gas with systematically different properties to that traced by narrow absorption: this gas is more diffuse, and less of the HI has been converted into either the CNM or into  $\text{H}_2$ . The conditions of this gas are closer to the threshold of the atomic-to-molecular transition; for example, see Zone C in Figure 3 of Bellomi et al. (2020), where both the molecular column densities and molecular fraction are comparable to the broad components analyzed in this work. In contrast to Bellomi et al. (2020), who considered only atomic and molecular column densities integrated along each line of sight, the spectral analysis we present here allows us to isolate the more-diffuse molecular gas from the denser components along a given line of sight and characterize the properties of this transition-state gas directly.

### 5.2.2. Comparison to broad, CO-dark OH emission

While we can infer the probable existence of multiple velocity components within the diffuse, CO-dark (or CO-dark\*) molecular gas traced by broad  $\text{HCO}^+$  absorption, the small-scale spatial structure of this very diffuse molecular gas remains unknown. The observations prevented here cannot distinguish between extended, extremely diffuse gas components of  $n(\text{H}_2) \sim 0.05 \text{ cm}^{-3}$  (e.g., Liszt & Lucas 2000; Busch et al. 2021), or an ensemble of smaller, denser gas structures (although comparisons to  $\text{HCO}^+$  emission do place limits on how dense  $\text{HCO}^+$  clumps can be; Lucas & Liszt 1996; Liszt & Lucas 2000).

Given the qualitative similarities between the broad  $\text{HCO}^+$  absorption observed by Liszt & Lucas (2000) and Rybarczyk et al. (2022), and the broad OH emission observed by Busch et al. (2021), it is natural to wonder whether these signatures share a common origin. New observations of  $\text{HCO}^+$  absorption and OH emission in the same directions will be used to test whether broad  $\text{HCO}^+$  absorption and broad OH emission are associated (Busch et al., in prep.). Further, because the OH emission beam is much larger than the  $\text{HCO}^+$  absorption pencil-beam, a comparison of the line profiles for the two tracers can be used to constrain the spatial distribution of the diffuse molecular gas producing the broad spectral signatures, thereby providing insight into the structure of the ISM near the atomic-to-molecular transition.

Future work will further use all of these spectral line observations (HI absorption and emission;  $\text{HCO}^+$  absorption; and CO absorption and emission; as well as new observations of OH emission and absorption in these directions) to constrain the physical and chemical properties of all diffuse gas clouds detected along each line of sight (see Wenger 2024). With multiple molecular gas species tracing the broad absorption, we will be able to place tight constraints on the gas kinetic temperature and level of turbulence. From the HI emission and absorption, we will also be able to constrain the temperature of the HI structures associated with broad absorption (previous attempts were unable to constrain the temperature of several components, e.g., Murray et al. 2018). This decomposition is beyond the scope of this work, and requires upcoming OH emission and absorption observations (Busch et al., in prep.).

### 5.3. Association with Galactic structure and kinematics

As discussed above, one of the defining attributes of CO-dark\* (or CO-dark)  $\text{HCO}^+$  absorption — as well as OH emission (Busch et al. 2021) — is the breadth of the profile in velocity (Liszt & Lucas 2000; Rybarczyk et al. 2022). The spectral profile is set by a combination of the local environmental conditions, Galactic rotation, the spatial distribution of gas along the line of sight, and local velocity perturbations. While we have discussed the abundance and excitation conditions in detail here, a full description of the origin of the diffuse molecular gas traced by broad  $\text{HCO}^+$  absorption will ultimately require constraints on the spatial distribution and kinematics of the diffuse ISM in any given direction. For example, does the fact that almost all of the narrow  $\text{HCO}^+$  absorption components identified in this work are flanked by broad  $\text{HCO}^+$  absorption at both positive

and negative velocities (see Figure 2) indicate a physical association of the gas traced by broad and narrow absorption?

Here we attempt to constrain the Galactocentric radii and kinematic distances to absorbing gas structures using the Markov Chain Monte Carlo technique developed by Wenger et al. (2018) implemented in the `kd` software package<sup>6</sup>. We note, though, that the typical uncertainties for both quantities are several hundred parsecs in these directions, (which do not account for the uncertainty in the reliability of kinematic distances at high Galactic latitudes), so it is difficult to conclude anything about the 3D spatial distribution of diffuse molecular gas in detail from our absorption spectra alone. Moreover, because we cannot map diffuse  $\text{HCO}^+$  in absorption and because the filling factor of the diffuse molecular gas traced by broad  $\text{HCO}^+$  absorption is unknown, it remains challenging to connect our spectra to structures in the recent 3D maps of the local ISM (e.g., Edenhofer et al. 2024), except for strongly-absorbing molecular clouds in these directions. For these structures, we find that kinematic distances are consistent within uncertainties, but such uncertainties large (a significant fraction of the distance). So while the kinematic distance analysis may provide clues to the large-scale spatial structure of diffuse molecular gas (see below), we argue that more work is needed to constrain the detailed spatial distribution of this gas — key to understanding its physical origin.

Two of our sightlines — 3C111 ( $\ell = 161.8^\circ$ ) and 3C120 ( $\ell = 190.4^\circ$ ) — point toward the outer Galaxy. At the observed velocities, the gas in the direction of these sources may trace the local arm, the Perseus arm, or perhaps even the Outer arm, with Galactocentric radii  $R_\odot \lesssim R \lesssim 12$  kpc. Given that the presence of  $\text{HCO}^+$  absorption is nearly continuous across a wide velocity range in each direction, there could also be a contribution from inter-arm gas (in the case of 3C111, at least it is clear that the spectrum comprises far greater than three discrete components). At a longitude of  $\ell = 86.1^\circ$ , the sightline toward 3C454.3 lies nearly parallel to the direction of Galactic rotation. This direction, too, probes mostly gas in the outer Galaxy, with  $R_\odot \lesssim R \lesssim 10$  kpc. These directions all probe gas at slightly lower metallicity (e.g., Esteban & García-Rojas 2018; Hawkins 2023). Busch et al. (2021) showed that significant CO-dark\* gas exists in the outer Galaxy (without absorption, they could not distinguish between CO-dark\* and CO-dark), which could be evidence for a

<sup>6</sup> <https://github.com/tvwenger/kd>

widespread thick disk ( $-200 \text{ pc} \lesssim z \lesssim 200 \text{ pc}$ ) of diffuse molecular gas. The near-continuous velocity coverage of  $\text{HCO}^+$  absorption we see toward 3C111, 3C120, and 3C454.3 is consistent with widespread diffuse molecular gas at  $R_\odot \lesssim R \lesssim 12 \text{ kpc}$ , consistent with the contention of Busch et al. (2021), but our sample size and lack of spatial information make it difficult to say anything global.

Meanwhile, J2023+335 and NRAO 530 point toward the inner Galaxy. J2023+335 is still reasonably close to the direction of Galactic rotation ( $\ell = 73.1^\circ$ ), so despite the kinematic distance ambiguity, the velocities of the observed molecular gas imply that most of this absorption is associated with the local arm and perhaps the Perseus arm. However, NRAO 530 is at low Galactic longitude ( $\ell = 12.0^\circ$ ), so this absorption may be local or may come from the far side of the Galaxy (though this is less likely, since at  $b = 10.1^\circ$ , the molecular gas would be at  $z \approx 300 \text{ pc}$  off the plane, well beyond the scale height of dense or diffuse molecular gas, e.g., Su et al. 2021). In either case, though, the Galactocentric radii are  $R_g \approx (7\text{--}9) \text{ kpc}$ .

## 6. CONCLUSIONS

Because molecular hydrogen is simultaneously the most important molecule in the ISM and extremely difficult to detect in many cold environments, our understanding of the molecular content of galaxies is biased by the imperfect observational approaches we must use to trace  $\text{H}_2$  indirectly. Although CO (the second most abundant molecule in galaxies) is often used to trace  $\text{H}_2$ , the existence of “CO-dark gas” — molecular gas without detectable CO emission (or, in this work, CO absorption) — is well established, especially in the diffuse ISM.

Here, we have investigated the atomic and molecular gas properties of CO-dark\* (and the stricter CO-dark; Table 1) gas associated with a particular spectral signature that has been highlighted in recent literature (Liszt & Lucas 2000; Rybarczyk et al. 2022, 2023; see also Busch et al. 2021), namely, kinematically broad  $\text{HCO}^+$  absorption observed toward diffuse sightlines. Our observations of sensitive CO absorption have enabled a direct comparison of the  $\text{HCO}^+$  and CO; previous work primarily compared broad  $\text{HCO}^+$  absorption to CO emission (Rybarczyk et al. 2022), which is less sensitive and probes different physical scales than CO pencil-beam absorption observations. We have also used sensitive HI absorption observations (including both new and archival data; Murray et al. 2018) to characterize the multiphase atomic gas in these directions.

We detect almost no CO absorption from the gas traced by broad  $\text{HCO}^+$  absorption, while we detect CO absorption associated with all of the narrow  $\text{HCO}^+$  features (Figures 1 and 2). Nevertheless, we do not find evidence that the CO abundance is systematically lower for the gas traced by broad absorption — the CO abundance (relative to  $\text{H}_2$ ) is  $\sim \text{few} \times 10^{-7}$  to  $\sim 10^{-5}$  for narrow absorption, and  $\lesssim \text{few} \times 10^{-6}$  (upper limits) for the broad absorption. Though significantly lower than the  $\sim 10^{-4}$  abundance in classic CO-bright molecular clouds (e.g., Federman et al. 1990; Liu et al. 2013), even the narrow absorption traces relatively diffuse gas in almost all cases (see Figures 4 and 7), and these abundances are consistent with model predictions (Wolfire et al. 2010). We further show that, for diffuse molecular gas with  $\text{few} \times 10^{18} \text{ cm}^{-2} \lesssim N(\text{H}_2) \lesssim 7 \times 10^{19} \text{ cm}^{-2}$ ,  $\text{HCO}^+$  absorption is likely to be detected in regions where neither CO emission or CO absorption could be detected with existing facilities (see Figure 8). Thus, in environments close to the atomic-to-molecular transition (e.g., Bellomi et al. 2020), CO is an ineffective tracer of  $\text{H}_2$ , while  $\text{HCO}^+$  absorption (and perhaps other tracers like OH emission, e.g., Busch et al. 2021; Busch 2024) are essential for characterizing this crucial phase in the evolution of gas in galaxies.

The gas traced by broad, CO-dark $\text{HCO}^+$  absorption has systematically different properties than the CO-bright (or merely CO-dark\*) gas in the same directions. The atomic gas coincident with broad  $\text{HCO}^+$  absorption has a lower CNM fraction than that associated with narrow  $\text{HCO}^+$  absorption (Figure 6). The fraction of hydrogen in the form of  $\text{H}_2$  is also lower for the gas associated with broad  $\text{HCO}^+$  absorption (Figure 7). As previously suggested by Rybarczyk et al. (2022), this could indicate that broad  $\text{HCO}^+$  absorption traces gas at the earliest stages of molecule formation in the diffuse ISM.

Yet, we argue that our observations suggest that the separation of broad and narrow absorption (Liszt & Lucas 2000; Rybarczyk et al. 2022) does not reflect a meaningful kinematic difference — the “broad” component simply traces *more diffuse* molecular gas (likely comprised in reality of multiple narrower components) where the  $\text{H}_2$  column density tends to be lower and CO is thus less likely to be detected in either emission or absorption, but where  $\text{HCO}^+$  remains detectable. Indeed, broad and narrow components at similar column densities show similar general properties.

Ultimately, it will be necessary to consider the atomic and molecular gas along each line of sight on a cloud-by-cloud basis. Future work comparing broad  $\text{HCO}^+$  absorption and a similar signature detected in OH emission (Liszt & Lucas 2000; Busch et al. 2021) may help

uncover the nature and physical origin of the broad signature. For example, it remains unclear from this work if the diffuse gas traced by broad HCO<sup>+</sup> emission belongs to a widespread, diffuse phase (e.g., Busch et al. 2021), or perhaps an ensemble of small, denser clumps. A full spectral decomposition of atomic and molecular observations in these directions will help us to constrain the physical sizes of clouds seen in emission and absorption, as well as characterize their physical and chemical properties on a cloud-by-cloud basis. This work awaits new observations of OH emission (which samples larger physical scales than the HCO<sup>+</sup> pencil-beam) and absorption, which will provide essential alternative probes of the diffuse molecular gas in these directions (Busch et al., in prep.).

The authors acknowledge Interstellar Institute’s programs “II6” and “II7” and the Paris-Saclay University’s Institut Pascal for hosting discussions that nourished the development of the ideas behind this work. D.R.R. is supported by a National Science Foundation Astronomy and Astrophysics Postdoctoral Fellowship under award AST-2303902. M.P.B. is supported by a Jansky Fellowship provided by the National Radio Astronomy Observatory. The National Radio Astronomy Observatory and Green Bank Observatory are facilities of the U.S. National Science Foundation operated under cooperative agreement by Associated Universities, Inc. This work is based on observations carried out under project number W21AC and W24BG with the IRAM NOEMA Interferometer. IRAM is supported by INSU/CNRS (France), MPG (Germany) and IGN (Spain). This paper makes use of the following ALMA data: ADS/JAO.ALMA#2018.1.00585.S and ADS/JAO.ALMA#2019.1.01809.S.. ALMA is a partnership of ESO (representing its member states), NSF (USA) and NINS (Japan), together with NRC (Canada), MOST and ASIAA (Taiwan), and KASI (Republic of Korea), in cooperation with the Republic of Chile. The Joint ALMA Observatory is operated by ESO, AUI/NRAO and NAOJ. This work benefited from the conference “Structure and polarization in the interstellar medium: A Conference in Honor of Prof. John Dickey”, a hybrid meeting hosted jointly at Stanford University and at the Australia Telescope National Facility in February 2025. We acknowledge support from the National Science Foundation (NSF Award No. 2502957), from the Kavli Institute for Particle Astrophysics and Cosmology, from the Commonwealth Scientific and Industrial Research Organisation, and from the Australian Research Council. We would also like to thank I. Grenier, M. Gong, and Y. Komichi for useful discussions regarding the content of this paper.

## REFERENCES

- Allen, R. J., Hogg, D. E., & Engelke, P. D. 2015, *AJ*, 149, 123, doi: [10.1088/0004-6256/149/4/123](https://doi.org/10.1088/0004-6256/149/4/123)
- Bellomi, E., Godard, B., Hennebelle, P., et al. 2020, *A&A*, 643, A36, doi: [10.1051/0004-6361/202038593](https://doi.org/10.1051/0004-6361/202038593)
- Bigiel, F., Leroy, A., Walter, F., et al. 2008, *AJ*, 136, 2846, doi: [10.1088/0004-6256/136/6/2846](https://doi.org/10.1088/0004-6256/136/6/2846)
- Bolatto, A. D., Wolfire, M., & Leroy, A. K. 2013, *ARA&A*, 51, 207, doi: [10.1146/annurev-astro-082812-140944](https://doi.org/10.1146/annurev-astro-082812-140944)
- Busch, M. P. 2024, *ApJ*, 967, 148, doi: [10.3847/1538-4357/AD3AF6](https://doi.org/10.3847/1538-4357/AD3AF6)
- Busch, M. P., Allen, R. J., Engelke, P. D., et al. 2019, *ApJ*, 883, 158, doi: [10.3847/1538-4357/ab3a4b](https://doi.org/10.3847/1538-4357/ab3a4b)
- Busch, M. P., Engelke, P. D., Allen, R. J., & Hogg, D. E. 2021, *ApJ*, 914, 72, doi: [10.3847/1538-4357/abf832](https://doi.org/10.3847/1538-4357/abf832)
- Cazaux, S., & Tielens, A. G. G. M. 2002, *ApJL*, 575, L29, doi: [10.1086/342607](https://doi.org/10.1086/342607)
- Dame, T. M., Hartmann, D., & Thaddeus, P. 2001, *ApJ*, 547, 792, doi: [10.1086/318388](https://doi.org/10.1086/318388)
- Dame, T. M., & Thaddeus, P. 2022, *ApJS*, 262, 5, doi: [10.3847/1538-4365/ac7e53](https://doi.org/10.3847/1538-4365/ac7e53)

- Donate, E., & Magnani, L. 2017, *MNRAS*, 472, 3169, doi: [10.1093/mnras/stx2211](https://doi.org/10.1093/mnras/stx2211)
- Edenhofer, G., Zucker, C., Frank, P., et al. 2024, *A&A*, 685, A82, doi: [10.1051/0004-6361/202347628](https://doi.org/10.1051/0004-6361/202347628)
- Esteban, C., & García-Rojas, J. 2018, *Monthly Notices of the Royal Astronomical Society*, 478, 2315, doi: [10.1093/mnras/sty1168](https://doi.org/10.1093/mnras/sty1168)
- Federman, S. R., Huntress, Jr., W. T., & Prasad, S. S. 1990, *ApJ*, 354, 504, doi: [10.1086/168711](https://doi.org/10.1086/168711)
- Gildas Team. 2013, GILDAS: Grenoble Image and Line Data Analysis Software, Astrophysics Source Code Library, record ascl:1305.010. <http://ascl.net/1305.010>
- Godard, B., Falgarone, E., Gerin, M., Hily-Blant, P., & de Luca, M. 2010, *A&A*, 520, A20, doi: [10.1051/0004-6361/201014283](https://doi.org/10.1051/0004-6361/201014283)
- Goldsmith, P. F. 2013, *ApJ*, 774, 134, doi: [10.1088/0004-637X/774/2/134](https://doi.org/10.1088/0004-637X/774/2/134)
- Goldsmith, P. F., Li, D., & Krčo, M. 2007, *ApJ*, 654, 273, doi: [10.1086/509067](https://doi.org/10.1086/509067)
- Green, G. M., Schlafly, E., Zucker, C., Speagle, J. S., & Finkbeiner, D. 2019, *ApJ*, 887, 93, doi: [10.3847/1538-4357/ab5362](https://doi.org/10.3847/1538-4357/ab5362)
- Güver, T., & Özel, F. 2009, *MNRAS*, 400, 2050, doi: [10.1111/j.1365-2966.2009.15598.x](https://doi.org/10.1111/j.1365-2966.2009.15598.x)
- Hafner, A., Dawson, J. R., Nguyen, H., et al. 2023, *PASA*, 40, e015, doi: [10.1017/pasa.2023.8](https://doi.org/10.1017/pasa.2023.8)
- Hawkins, K. 2023, *Monthly Notices of the Royal Astronomical Society*, 525, 3318, doi: [10.1093/mnras/stad1244](https://doi.org/10.1093/mnras/stad1244)
- Heiles, C., & Troland, T. H. 2003, *ApJS*, 145, 329, doi: [10.1086/367785](https://doi.org/10.1086/367785)
- Kaufman, M. J., Wolfire, M. G., & Hollenbach, D. J. 2006, *ApJ*, 644, 283, doi: [10.1086/503596](https://doi.org/10.1086/503596)
- Kim, C.-G., Ostriker, E. C., & Kim, W.-T. 2014, *ApJ*, 786, 64, doi: [10.1088/0004-637X/786/1/64](https://doi.org/10.1088/0004-637X/786/1/64)
- Li, D., Tang, N., Nguyen, H., et al. 2018, *ApJS*, 235, 1, doi: [10.3847/1538-4365/aaa762](https://doi.org/10.3847/1538-4365/aaa762)
- Liszt, H., & Gerin, M. 2023a, *A&A*, 675, A145, doi: [10.1051/0004-6361/202346259](https://doi.org/10.1051/0004-6361/202346259)
- . 2023b, *ApJ*, 943, 172, doi: [10.3847/1538-4357/acae83](https://doi.org/10.3847/1538-4357/acae83)
- Liszt, H., Gerin, M., & Grenier, I. 2019, *A&A*, 627, A95, doi: [10.1051/0004-6361/201935436](https://doi.org/10.1051/0004-6361/201935436)
- Liszt, H., & Lucas, R. 2000, *A&A*, 355, 333
- Liszt, H., Lucas, R., & Pety, J. 2005, in *Astrochemistry: Recent Successes and Current Challenges*, ed. D. C. Lis, G. A. Blake, & E. Herbst, Vol. 231, 187–196, doi: [10.1017/S1743921306007186](https://doi.org/10.1017/S1743921306007186)
- Liszt, H. S. 2017, *ApJ*, 835, 138, doi: [10.3847/1538-4357/835/2/138](https://doi.org/10.3847/1538-4357/835/2/138)
- Liszt, H. S., & Lucas, R. 1998, *A&A*, 339, 561
- Liszt, H. S., & Pety, J. 2012, *A&A*, 541, A58, doi: [10.1051/0004-6361/201218771](https://doi.org/10.1051/0004-6361/201218771)
- Liszt, H. S., Pety, J., Gerin, M., & Lucas, R. 2014, *A&A*, 564, A64, doi: [10.1051/0004-6361/201323320](https://doi.org/10.1051/0004-6361/201323320)
- Liu, T., Wu, Y., & Zhang, H. 2013, *ApJL*, 775, L2, doi: [10.1088/2041-8205/775/1/L2](https://doi.org/10.1088/2041-8205/775/1/L2)
- Lucas, R., & Liszt, H. 1996, *A&A*, 307, 237
- Luo, G., Li, D., Tang, N., et al. 2020, *ApJL*, 889, L4, doi: [10.3847/2041-8213/ab6337](https://doi.org/10.3847/2041-8213/ab6337)
- Luo, G., Zhang, Z.-Y., Bisbas, T. G., et al. 2023, *ApJ*, 946, 91, doi: [10.3847/1538-4357/acbf34](https://doi.org/10.3847/1538-4357/acbf34)
- Luo, G., Li, D., Zhang, Z.-Y., et al. 2024, *A&A*, 685, L12, doi: [10.1051/0004-6361/202450067](https://doi.org/10.1051/0004-6361/202450067)
- McClure-Griffiths, N. M., Stanimirović, S., & Rybarczyk, D. R. 2023, *ARA&A*, 61, 19, doi: [10.1146/annurev-astro-052920-104851](https://doi.org/10.1146/annurev-astro-052920-104851)
- McClure-Griffiths, N. M., Pisano, D. J., Calabretta, M. R., et al. 2009, *ApJS*, 181, 398, doi: [10.1088/0067-0049/181/2/398](https://doi.org/10.1088/0067-0049/181/2/398)
- Murray, C. E., Stanimirović, S., Goss, W. M., et al. 2018, *ApJS*, 238, 14, doi: [10.3847/1538-4365/aad81a](https://doi.org/10.3847/1538-4365/aad81a)
- Murray, C. E., Stanimirović, S., Heiles, C., et al. 2021, *ApJS*, 256, 37, doi: [10.3847/1538-4365/ac0f0b](https://doi.org/10.3847/1538-4365/ac0f0b)
- Murray, C. E., Stanimirović, S., Goss, W. M., et al. 2015, *ApJ*, 804, 89, doi: [10.1088/0004-637X/804/2/89](https://doi.org/10.1088/0004-637X/804/2/89)
- Nguyen, H., Dawson, J. R., Lee, M.-Y., et al. 2019, *ApJ*, 880, 141, doi: [10.3847/1538-4357/ab2b9f](https://doi.org/10.3847/1538-4357/ab2b9f)
- Nguyen, H., Dawson, J. R., Miville-Deschênes, M.-A., et al. 2018, *ApJ*, 862, 49, doi: [10.3847/1538-4357/aac82b](https://doi.org/10.3847/1538-4357/aac82b)
- Park, G., Lee, M.-Y., Bialy, S., et al. 2023, *ApJ*, 955, 145, doi: [10.3847/1538-4357/ace164](https://doi.org/10.3847/1538-4357/ace164)
- Peek, J. E. G., Heiles, C., Douglas, K. A., et al. 2011, *ApJS*, 194, 20, doi: [10.1088/0067-0049/194/2/20](https://doi.org/10.1088/0067-0049/194/2/20)
- Peek, J. E. G., Babler, B. L., Zheng, Y., et al. 2018, *ApJS*, 234, 2, doi: [10.3847/1538-4365/aa91d3](https://doi.org/10.3847/1538-4365/aa91d3)
- Pety, J. 2005, in *SF2A-2005: Semaine de l’Astrophysique Française*, ed. F. Casoli, T. Contini, J. M. Hameury, & L. Pagani, 721
- Rybarczyk, D. R., Stanimirović, S., & Gusdorf, A. 2023, *ApJ*, 950, 52, doi: [10.3847/1538-4357/acbba1](https://doi.org/10.3847/1538-4357/acbba1)
- Rybarczyk, D. R., Stanimirović, S., Gong, M., et al. 2022, *ApJ*, 928, 79, doi: [10.3847/1538-4357/ac5035](https://doi.org/10.3847/1538-4357/ac5035)
- Schlafly, E. F., & Finkbeiner, D. P. 2011, *ApJ*, 737, 103, doi: [10.1088/0004-637X/737/2/103](https://doi.org/10.1088/0004-637X/737/2/103)
- Sheffer, Y., Rogers, M., Federman, S. R., et al. 2008, *ApJ*, 687, 1075, doi: [10.1086/591484](https://doi.org/10.1086/591484)
- Stanimirović, S., Murray, C. E., Lee, M.-Y., Heiles, C., & Miller, J. 2014, *ApJ*, 793, 132, doi: [10.1088/0004-637X/793/2/132](https://doi.org/10.1088/0004-637X/793/2/132)

- Su, Y., Yang, J., Yan, Q.-Z., et al. 2021, *ApJ*, 910, 131, doi: [10.3847/1538-4357/abe5ab](https://doi.org/10.3847/1538-4357/abe5ab)
- Wenger, T. 2024, *The Journal of Open Source Software*, 9, 7201, doi: [10.21105/joss.07201](https://doi.org/10.21105/joss.07201)
- Wenger, T. V., Balser, D. S., Anderson, L. D., & Bania, T. M. 2018, *ApJ*, 856, 52, doi: [10.3847/1538-4357/aaec8](https://doi.org/10.3847/1538-4357/aaec8)
- Wolfire, M. G., Hollenbach, D., & McKee, C. F. 2010, *ApJ*, 716, 1191, doi: [10.1088/0004-637X/716/2/1191](https://doi.org/10.1088/0004-637X/716/2/1191)
- Xu, D., Li, D., Yue, N., & Goldsmith, P. F. 2016, *ApJ*, 819, 22, doi: [10.3847/0004-637X/819/1/22](https://doi.org/10.3847/0004-637X/819/1/22)
- Zhu, H., Tian, W., Li, A., & Zhang, M. 2017, *MNRAS*, 471, 3494, doi: [10.1093/mnras/stx1580](https://doi.org/10.1093/mnras/stx1580)